International Association of Geodesy Symposia
139

Chris Rizos
Pascal Willis *Editors*

Earth on the Edge: Science for a Sustainable Planet

Proceedings of the IAG General Assembly, Melbourne, Australia, June 28 – July 2, 2011

Springer

International Association of Geodesy Symposia

Chris Rizos, Series Editor
Pascal Willis, Assistant Series Editor

For further volumes:
http://www.springer.com/series/1345

International Association of Geodesy Symposia

Chris Rizos, Series Editor
Pascal Willis, Assistant Series Editor

Symposium 101: Global and Regional Geodynamics
Symposium 102: Global Positioning System: An Overview
Symposium 103: Gravity, Gradiometry, and Gravimetry
Symposium 104: Sea SurfaceTopography and the Geoid
Symposium 105: Earth Rotation and Coordinate Reference Frames
Symposium 106: Determination of the Geoid: Present and Future
Symposium 107: Kinematic Systems in Geodesy, Surveying, and Remote Sensing
Symposium 108: Application of Geodesy to Engineering
Symposium 109: Permanent Satellite Tracking Networks for Geodesy and Geodynamics
Symposium 110: From Mars to Greenland: Charting Gravity with Space and Airborne Instruments
Symposium 111: Recent Geodetic and Gravimetric Research in Latin America
Symposium 112: Geodesy and Physics of the Earth: Geodetic Contributions to Geodynamics
Symposium 113: Gravity and Geoid
Symposium 114: Geodetic Theory Today
Symposium 115: GPS Trends in Precise Terrestrial, Airborne, and Spaceborne Applications
Symposium 116: Global Gravity Field and Its Temporal Variations
Symposium 117: Gravity, Geoid and Marine Geodesy
Symposium 118: Advances in Positioning and Reference Frames
Symposium 119: Geodesy on the Move
Symposium 120: Towards an Integrated Global Geodetic Observation System (IGGOS)
Symposium 121: Geodesy Beyond 2000: The Challenges of the First Decade
Symposium 122: IV Hotine-Marussi Symposium on Mathematical Geodesy
Symposium 123: Gravity, Geoid and Geodynamics 2000
Symposium 124: Vertical Reference Systems
Symposium 125: Vistas for Geodesy in the New Millennium
Symposium 126: Satellite Altimetry for Geodesy, Geophysics and Oceanography
Symposium 127: V Hotine Marussi Symposium on Mathematical Geodesy
Symposium 128: A Window on the Future of Geodesy
Symposium 129: Gravity, Geoid and Space Missions
Symposium 130: Dynamic Planet - Monitoring and Understanding . . .
Symposium 131: Geodetic Deformation Monitoring: From Geophysical to Engineering Roles
Symposium 132: VI Hotine-Marussi Symposium on Theoretical and Computational Geodesy
Symposium 133: Observing our Changing Earth
Symposium 134: Geodetic Reference Frames
Symposium 135: Gravity, Geoid and Earth Observation
Symposium 136: Geodesy for Planet Earth
Symposium 137: VII Hotine-Marussi Symposium on Mathematical Geodesy
Symposium 138: Reference Frames for Applications in Geosciences

Earth on the Edge: Science for a Sustainable Planet

Proceedings of the IAG General Assembly, Melbourne, Australia, June 28 - July 2, 2011

Edited by

Chris Rizos
Pascal Willis

Springer

Volume Editors
Chris Rizos
School of Surveying
University of New South Wales
Sydney
Australia

Pascal Willis
Institut national de l'Information
Geographique et Forestiere
Direction Technique
Saint-Mande
France

Series Editor
Chris Rizos
School of Surveying
University of New South Wales
Sydney
Australia

Assistant Series Editor
Pascal Willis
Institut national de l'Information
Geographique et Forestiere
Direction Technique
Saint-Mande
France

ISSN 0939-9585
ISBN 978-3-642-37221-6 ISBN 978-3-642-37222-3 (eBook)
DOI 10.1007/978-3-642-37222-3
Springer Heidelberg New York Dordrecht London

Library of Congress Control Number: 2013956350

Preface

At the XXV General Assembly of the International Union of Geodesy and Geophysics (IUGG), held from June 27 to July 8, 2011 in Melbourne, Australia, the International Association of Geodesy (IAG) also had its quadrennial General Assembly. The IAG co-organised and contributed to several Union Symposia, as well as to Joint Symposia with other Associations. It also organised seven symposia of its own, one dedicated to each of the four commissions and three dedicated to specific scientific issues. This volume contains the proceedings of 13 symposia, which are listed below with the name of their associate editor(s):

Symposium JG01: Space Geodesy-based Atmospheric Remote Sensing as a Synergistic Link between Geodesy and Meteorology
Editors: Marcelo Santos, Jens Wickert

Symposium JG02: Application of Geodetic Techniques in Cryospheric Studies
Editor: Reinhard Dietrich, Matt King

Symposium JG03: History of Geosciences from Terrestrial to Spaceborne Observations
Editor: Jozsef Adàm

Symposium JG04: Structure and Deformation of Plate Interiors
Editor: John Dawson

Symposium JG05: Integrated Earth Observing Systems
Editor: Markus Rothacher

Symposium JG06: Tectonic Geodesy and Earthquakes
Editor: Jeff Freymueller

Symposium G01: Reference Frames from Regional to Global Scales
Editor: Zuheir Altamimi, Athanasios Dermanis, Joao Agria Torres

Symposium G02: Monitoring and Modelling of Mass Distribution and Mass Displacements by Geodetic Methods
Editors: Yoichi Fukuda, Nico Sneeuw, Frank Lemoine, Richard Gross, Herbert Wilmes

Symposium G03: Monitoring and Modelling Earth Rotation
Editors: Richard Gross, Harald Schuh, Oleg Titov

Symposium G04: Multisensor Systems for Engineering Geodesy
Editors: Dorota Grejner-Brzezinska, Hanjörg Kutterer

Symposium G05: Geodetic Imaging Techniques
Editor: Sandra Verhagen, Xiaoli Ding

Symposium G06: Towards a Unified World Height System
Editors: Johannes Ihde, Laura Sanchez

Symposium G07: High Precision GNSS
Editors: Urs Hugentobler, Mikael Lilje, Ruth Neilan

The goal of Modern Geodesy is to monitor changes in a range of physical processes in the solid Earth, the atmosphere and the oceans in order to improve our understanding of this fragile, precious and stressed planet. This is an ambitious goal, but one that all geodesists can have confidence that we are making significant progress in addressing. The range of papers presented at the IAG General Assembly is testament to the ingenuity and hard work of scientists and engineers engaged in geodetic studies and in operational geodesy. Although contributions to the so-called three pillars of geodesy—geometry,

Earth rotation and gravity field—are clearly evident, increasingly the authors of the papers are documenting the contributions of Modern Geodesy to science and society in the context of services and integrated observing systems. One notes that geodesy is applying state-of-the-art technologies (primarily, though not exclusively space-based) and methodologies to what amounts to "Earth Observation", that is the monitoring in space and time of a variety of Earth process parameters that have geometric, gravimetric or Earth rotation signatures. However, while Modern Geodesy is making enormous contributions to the geosciences as an Earth Observation science, geodesy continues to demonstrate its relevance to society in general, through the provision of fundamental reference frames, Earth observing systems and precise positioning capabilities.

The 2011 General Assembly attracted 370 geodesists from 44 countries. There were 264 oral presentations and 217 posters made at the seven IAG Symposia and six Joint IAG Symposia. Approximately 25 % of those contributions were submitted as full papers for peer review and inclusion in these proceedings. The 80 accepted papers are contained in this volume.

There are several colleagues who contributed to the success of the IAG General Assembly and should be acknowledged here. I am grateful to Hermann Drewes, the Secretary General of the IAG, who coordinated together with the IUGG and IAG Executive Committees and the Local Organising Committee the venue selection, as well as the scheduling and organisation of the symposia which IAG led or contributed to. Michael Sideris, the past President of the IAG, oversaw the planning of the IAG General Assembly. The symposia conveners and co-conveners from the IAG Commissions, Services, GGOS and the Inter-commission Committee on Theory listed on the previous page are gratefully acknowledged for the selection and organisation of the scientific content of the symposia.

Pascal Willis, the IAG Symposium Series Associate Editor, guided the reviews of the submitted papers, communicated with the symposium editors and the paper reviewers, and finally accepted the papers that comprise this volume. I am personally indebted to him, for I could not have put this volume together without his invaluable assistance and tenacity.

For the first time the complete review process (paper submission, review and acceptance) was carried out electronically using the new submission web site created by Springer: http://www.editorialmanager.com/iags.

Last, but definitively not least, I wish to sincerely thank all the participating scientists of all ages, and those who made oral and poster presentations, who came to Melbourne and made our General Assembly an unqualified success.

Sydney, NSW, Australia Chris Rizos
19 January 2013

Contents

Part I

JG01: Space Geodesy-Based Atmospheric Remote Sensing as a Synergistic Link Between Geodesy and Meteorology

Generation and Assessment of VMF1-Type Grids Using North-American Numerical Weather Models

Landon Urquhart, Marcelo C. Santos, Felipe G. Nievinski, and Johannes Böhm

Abstract

Numerical weather models (NWM) have become an important source of atmospheric data for modeling error sources in geodetic positioning. One example of this is the development of the Vienna Mapping Functions (VMF1) and ray-traced zenith delays which are derived from the European Centre for Medium-range Weather Forecasts (ECMWF) datasets. These products are provided on an operational basis through the GGOS Atmosphere project. In general, relatively little consideration has been given to the choice of NWM on the derived mapping functions and zenith delay products. In this investigation we compare the gridded-VMF1 mapping functions and ray-traced zenith delays derived from the ECMWF to equivalent products derived by ray-tracing through the National Center for Environmental Prediction (NCEP) Reanalysis model. We have chosen to compare the gridded version of these products as they are available for any location on Earth, rather than only specific stations and have been shown to be essentially equivalent in terms of accuracy. This paper also includes a discussion about a systematic production of gridded-VMF1 and ray-traced zenith delays derived from the NCEP datasets (and from the Canadian Meteorological Center GEM model) on an operational basis. The benefits of the service would include: (1) a backup in the event of the ECMWF VMF1 or zenith delays being unavailable; (2) greater compatibility with other NWM derived corrections, such as atmospheric pressure loading and; (3) the availability of tropospheric delay products derived from an independent source and ray-tracing algorithms should provide more robustness for combination products which use these models.

Keywords

Mapping functions • Neutral atmosphere • Tropospheric delay • Vienna Mapping Functions

1 Introduction

In recent years, numerical weather models have been used operationally to improve the accuracy of space geodetic techniques. The Vienna Mapping Function 1 (VMF1) Service, which falls under the Global Geodetic Observation System: Atmosphere (GGOS Atmosphere http://ggosatm.hg.tuwien.ac.at/), provides ray-traced zenith delays and slant factor models derived from numerical weather model data on a 6-h basis, which can then be applied

L. Urquhart • M.C. Santos (✉)
Department of Geodesy and Geomatics Engineering, University of New Brunswick, P.O. Box 4400, Fredericton, NB, Canada E3B 5A3
e-mail: msantos@unb.ca

F.G. Nievinski
Department of Aerospace Engineering Sciences, University of Colorado, Boulder, CO, USA

J. Böhm
Institute of Geodesy and Geophysics, Vienna University of Technology, Vienna, Austria

C. Rizos and P. Willis (eds.), *Earth on the Edge: Science for a Sustainable Planet*, International Association of Geodesy Symposia 139, DOI 10.1007/978-3-642-37222-3_1,

for modeling the tropospheric delays in space geodetic observations.

The VMF1 mapping functions have been shown to be the most accurate mapping function to date (Tesmer et al. 2007). They are currently recommended for all precise geophysical applications, in particular if geophysical signals are to be investigated (Boehm and van Dam 2009). At this time the processing centers contributing to the International GNSS Service (IGS) have not adopted the VMF1 in the operational analysis routines, which may be due to concerns in the products availability. The VMF1 mapping functions are recommended by the International Earth Rotation and Reference Systems Service (IERS) in their most recent publication of the IERS Conventions (Petit and Luzum 2010).

The provision of a UNB VMF1-like service would improve the availability of VMF1 mapping functions making it less likely of a disruption in the service. Additionally, the independent source of the VMF1 mapping functions and the ray-traced zenith delays may be beneficial in improving the robustness of the IGS/IERS combined products as it would provide an independent source for tropospheric corrections. A UNB service would also act as a basis for developing improved tropospheric products such as azimuth-dependent VMF1 or ray-traced slant factors at the observation level.

First, a review of the current VMF1 service is provided. Next, we describe the benefits to providing an alternative source of corrections to the geodetic community. Finally, we look into the implementation of the VMF1-like service, discussing the distribution to users, NWM data provider and ray-tracing algorithms.

2 VMF1 Service

This is the current state-of-the-art approach to modelling the troposphere delay as recommended by the latest IERS Conventions (Petit and Luzum 2010):

$$\Delta L = \Delta L_{\mathrm{h}}^{z} \cdot mf_{\mathrm{h}}(e) + \Delta L_{\mathrm{w}}^{z} \cdot mf_{\mathrm{w}}(e) + mf_{\mathrm{G}}(e) \cdot [G_{\mathrm{N}} \cdot \cos(\alpha) + G_{\mathrm{E}} \cdot \sin(\alpha)] \quad (1)$$

where ΔL is the total delay, the two ΔL^z represent the zenith delay for the hydrostatic ("dry") and non-hydrostatic ("wet") components (indicated by subscripts h and w, respectively), $mf\ (e)$ is the mapping function, as a function of the elevation angle e for the hydrostatic (subscript h), wet (subscript w) and for the gradient (subscript G). The two troposphere gradient parameters are represented by G_{N} and G_{E}, and α indicates the azimuth. The mapping function mf is the concern of this paper, and can be determined by the Vienna Mapping Functions 1.

Table 1 Coefficients for the VMF1 mapping function

Hemisphere	c_0	c_{10}	c_{11}	ψ
Northern	0.062	0.001	0.005	0
Southern	0.062	0.002	0.007	π

The VMF1 service relies on a numerical weather model produced by European Centre for Medium-range Weather Forecasts (ECMWF) and is implemented on the super-computing facilities of the ECMWF. The underlying functional formulation for describing the elevation angle dependence of the tropospheric delay is given by Marini (1972), normalized to yield unity at the zenith by Herring (1992):

$$mf(e) = \frac{1 + \frac{a}{1+\frac{b}{1+c}}}{\sin e + \frac{a}{\sin e + \frac{b}{\sin e + c}}} \quad (2)$$

In a preliminary fit, all a_{h}, b_{h}, and c_{h} coefficients for the hydrostatic mapping function are determined from a least-squares fit of ray-traced observations taken at nine elevation angles, through monthly mean profiles of the ECMWF 40-year reanalysis data to Eq. (1). Then the b_{h} coefficient is held fixed to its mean value, equal to 0.0029, while the c_{h} coefficient is re-fit to the expression:

$$c = c_0 + \left[\left(\cos\left(\frac{doy - 28}{365.25} 2\pi + \psi\right) + 1\right)\frac{c_{11}}{2} + c_{10}\right] \times (1 - \cos\phi) \quad (3)$$

where doy is the day-of-the-year, ψ specifies either the northern or southern hemisphere (values 0 and π, respectively), and φ is the station latitude. Bear in mind that the values of the coefficients as shown in Table 1 in (Boehm et al. 2006b) are not correct.

The b_{w} and c_{w} coefficients for the non-hydrostatic mapping function were deemed to be less important as the non-hydrostatic delay is typically ten times smaller than the hydrostatic and therefore the coefficients remain to be fixed to those of the NMF (Niell 1996) at the 45° elevation angle, where b_{w} and c_{w} equal 0.00146 and 0.04391 respectively.

The final a coefficient is determined by ray-tracing through the ECMWF analysis on a 6-h basis at an initial elevation angle of 3.3° and then inverting Eq. (2) with b and c fixed as above. In this case, the corresponding outgoing elevation angle, which should be equal to approximately 3°, must be determined from the ray-tracing procedure in order to solve for the a coefficient. This approach is used for both the hydrostatic and non-hydrostatic mapping functions.

Originally, the VMF1 was produced on a site-specific basis. However, this was seen as a limitation as it constrained its use to only those stations for which the coefficients were computed. For this reason, the VMF1-grid coefficients are produced to allow users to simply interpolate the coefficients to the required location. Kouba (2008) showed that the difference between the gridded and site VMF1 are negligible and therefore the VMF1-grid is more desirable as it can be applied for all locations.

In the case of the VMF1-grid, the *a* coefficients are provided on a $2.0° \times 2.5°$ latitude/longitude grid. They are computed every 6 h at 0, 6, 12, and 18 UTC at ellipsoidal heights corresponding to the grid nodes of a global topography model (file *orography_ell*). The *a* coefficients are then reduced to the ellipsoid and these "zero height" values are the ones provided to end-users; in order to apply them, the subroutine *vmf1_ht.m* (which is available at: http://ggosatm.hg.tuwien.ac.at/DELAY/SOURCE/) must be used which applies a height correction to determine the *a* coefficient for the actual station height. The height correction to obtain the coefficient at the actual station height during grid usage is simply the inverse of the height reduction to obtain the coefficients on the ellipsoid during grid generation.

In addition to the mapping function, the zenith hydrostatic and non-hydrostatic delays are also provided in the gridded format. The zenith delays are provided at mean grid heights corresponding to the ellipsoid height in *orography_ell* and the zenith delays must be corrected for the difference in the gridded height and the actual station height. Several options are available and they are discussed in Kouba (2008) and Fund et al. (2009). This correction is performed by the user and is not part of the VMF1-service.

3 The UNB VMF1 Implementation

The geodetic community is now in a transition from corrections based on relatively simple closed-form mathematical models to corrections based on large amounts of external data. The VMF1 service is only one example of this shift. Even though the VMF1 mapping functions have been shown to be an improvement over the Global Mapping Functions (Boehm et al. 2006a) and Niell Mapping Functions (Niell 1996), at this time they have not been widely adopted for operational use even though they are currently recommended by the IERS Conventions (Petit and Luzum 2010). An alternative service provider could improve the availability of the products should the original VMF service become unavailable and perhaps make the use of the VMF1 corrections more appealing.

An alternative source of mapping functions and ray-traced zenith delays could improve the robustness of the IGS/IERS combined solutions as it would provide an independent source of corrections which could be applied by the analysis centers. When producing the IGS combined products the results from all analysis centers are combined in a least squares approach, even though in reality many of these solutions are highly correlated due to applying the same correction models and some analysis centers even using the same software. A UNB VMF1-like service would provide slant factor models based on an independent weather model and ray-tracing algorithms which would make the IGS combined solution more robust if the IGS did choose to switch to the VMF1 for operational use.

As was shown in Urquhart (2010) there exists a small latitude dependent bias in the VMF1 hydrostatic mapping function which is believed to be due to the assumption of a sphere of constant radius of the earth in the ray-tracing algorithms. This systematic bias results in an approximately 2 mm change in station height at the poles and at the equator. Although small, this systematic bias may be important for geophysical studies and for establishing reference frames. This will be further discussed below.

The UNB VMF1-like implementation is based on NOAA-NCEP reanalysis for operational purposes, but can also utilize the CMC-GEM models for comparison and quality control. In this investigation Numerical weather data available at every 6 h is used and the gridded version of the VMF1/UNB-VMF1 is compared which uses a $2.0° \times 2.5°$ latitude/longitude grid. The same empirical expressions for the coefficients *b* and *c* were employed to maintain consistency with the original VMF1. The impact of this assumption on accuracy will be assessed in the future. Validation data was provided by using independent three dimensional ray-traced observations. The ray-tracing algorithms used in the UNB implementation of the VMF1 are those described in Nievinski (2009).

4 Assessment

Several tests were made in order to evaluate the UNB implementation of the VMF1. The data set considered covers the whole of 2010, at four epochs daily (every 6 h), unless otherwise stated.

4.1 Zenith Delay Comparisons

The first comparison involves zenith delays derived from the ECMWF and NCEP weather models. Figure 1 shows the zenith hydrostatic delay difference between a the VMF1 solution based on the ECMWF and the UNB solution based on NCEP re-analysis. There are several outliers present which cause the extended colour bar in both cases. At this time it was not determined which product was the

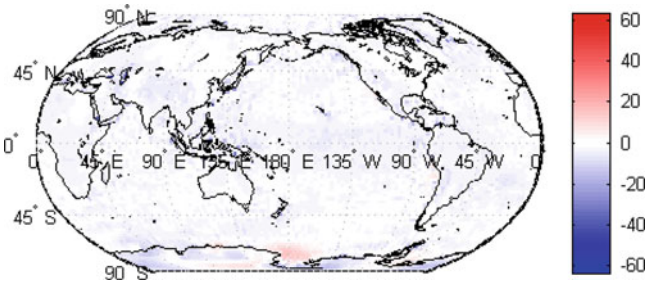

Fig. 1 Hydrostatic zenith delays (ECMWF − NCEP); *colour bar* in mm for the full year of 2010, four epochs daily

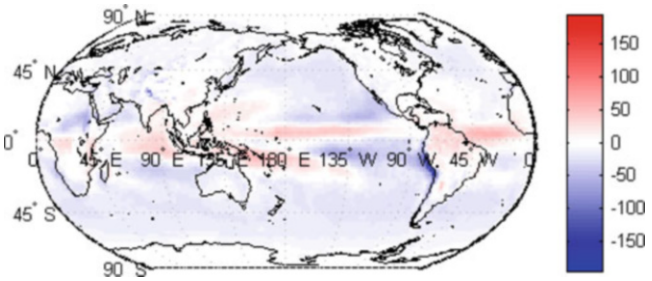

Fig. 2 Non-hydrostatic zenith delays (ECMWF − NCEP); *colour bar* in mm for the full year of 2010, four epochs daily

source of these outliers. For the hydrostatic delays there are several larger values occurring in Europe (and some also in Antarctica), while for the non-hydrostatic delay (shown in Fig. 2) the larger differences occur along the western coast of South America. There are some interesting effects in the equatorial region for the non-hydrostatic delays; most differences, though small, are over the oceans. Statistics for the hydrostatic delay are -2.4 ± 3.8 mm, whereas that for the non-hydrostatic delay it was found to be -6.3 ± 14.7 mm.

4.2 Comparison with Saastamoinen

A comparison using Saastamoinen (1972) zenith hydrostatic delay as truth is shown in Fig. 3, for 60 days (January and February, 2010). Input meteorological values were obtained from the station met files provided on the CDDIS data server. There is good agreement in the mean, but the UNB (NCEP) zenith hydrostatic delays tend to be noisier than the ECMWF zenith hydrostatic delays. This is believed to be due to the interpolation of the NCEP pressure levels fed to the UNB ray-tracer. Statistics contained in Table 2 are just for the stations shown in Fig. 3.

An analysis adding CMC zenith delays into the comparison was made for a 2-week period in 2008. In Fig. 4 we see the comparison of the zenith hydrostatic delay with respect to Saastamoinen. Notice that both the CMC and

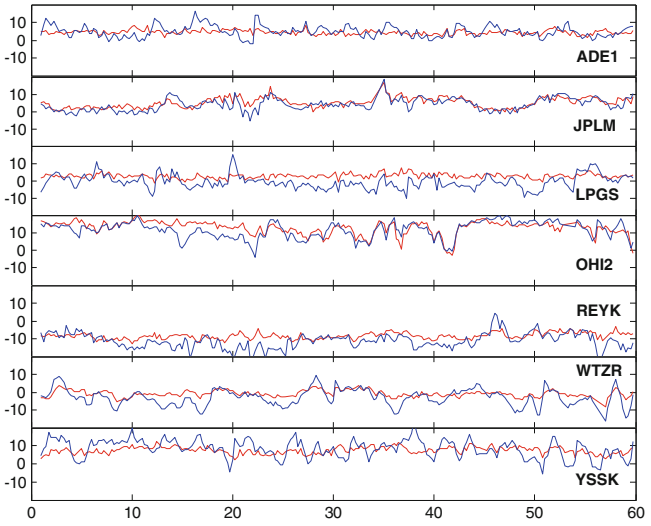

Fig. 3 Comparison with respect to Saastamoinen delays: *red* is for ECMWF (Vienna); *blue* is for NCEP (UNB). *Horizontal axis* indicates days, *vertical* is discrepancy in mm

Table 2 Average statistics over stations

Zenith hydrostatic delay	Bias	Standard deviation
ECMWF (Vienna)	3.3 mm	2.2 mm
NCEP (UNB)	2.0 mm	4.2 mm

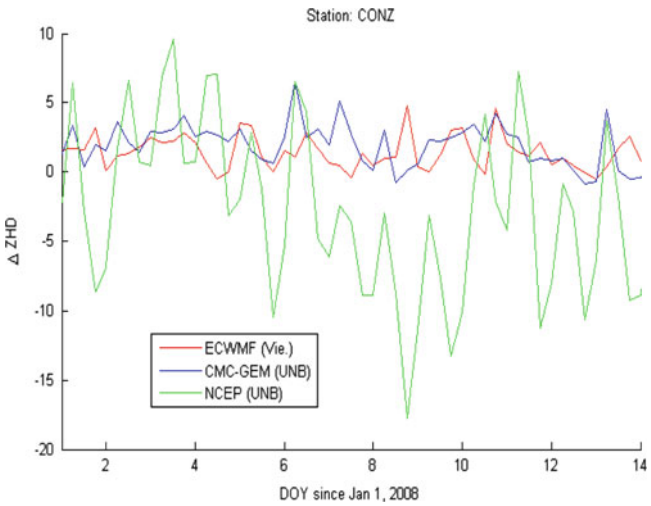

Fig. 4 Comparison with respect to Saastamoinen delays: *red* is for ECMWF (Vienna); *blue* is for CMC-GEM (UNB); and *green* for NCEP (UNB). *Horizontal axis* indicates days, *vertical* is discrepancy in mm

ECMWF results agree very well, both in bias and standard deviation with respect to the met-driven Saastamoinen. This was expected as we have performed significant more tests on the use of CMC in ray-tracing. Further work is required to identify the cause of the noisier results using NCEP.

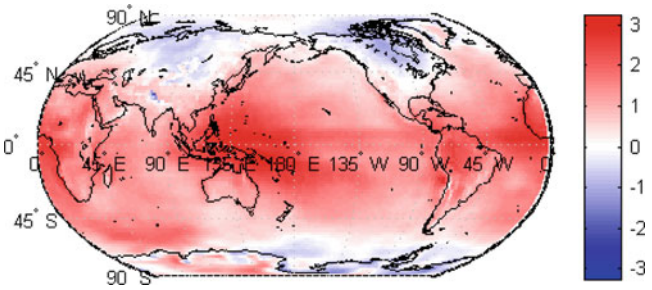

Fig. 5 Hydrostatic station height difference (ECMWF − NCEP); *colour bar* in mm

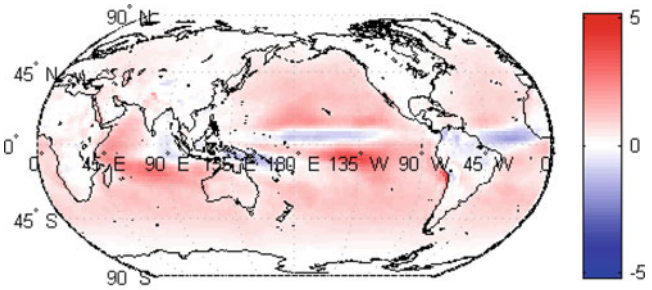

Fig. 6 Non-hydrostatic station height difference (ECMWF − NCEP); *colour bar* in mm

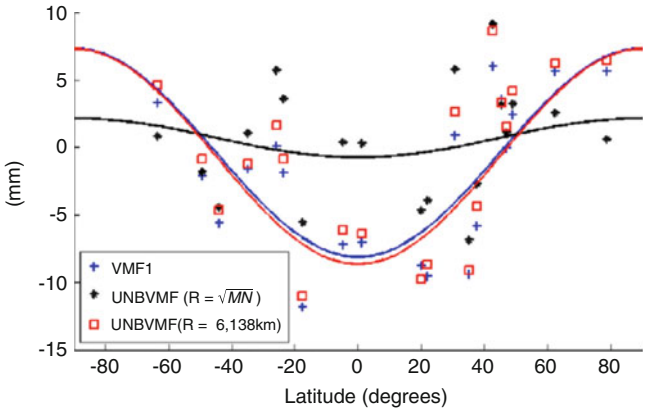

Fig. 7 Hydrostatic slant delay differences at the 5° elevation angle due to different radii of curvature. *Blue cross*: original VMF1, using a constant radius; *red squares*: UNB implementation using a constant radius; *black stars*: UNB implementation using the Gaussian radius. In this comparison, all UNB implementations used CMC-GEM data. The *lines* represent a least-squares fit of the data to the function $a{\cdot}\cos(2\phi) + c$. Values in mm

4.3 Comparison of Mapping Functions

In these comparisons the following rule of thumb (Boehm et al. 2008) is used: "bias in station height is approximately equal to 1/5 bias in slant delay at 5° elevation angle."

The difference in station height due to mapping functions are shown in Fig. 5 (for the hydrostatic) and in Fig. 6 (for the non-hydrostatic). It shows a very small bias for both components: $0.8 \pm 0.\ 9$ and 0.4 ± 0.6 mm, respectively. Notice that for the hydrostatic we see positive bias over the oceans and negative bias over land. Possible reasons for this, still in need of in-depth investigation, are: (a) the orography model used (currently we are using ECMWF orography); (b) partly due to differences in treatment of Earth's radius (see next paragraph).

The effect of Earth's radius on slant hydrostatic delay is discussed as follows. A local approximation to the ellipsoid can be represented by a normal sphere, i.e., whose radial direction coincides with the ellipsoid normal point on the surface. The radius of such a normal sphere can be computed in various ways. The most accurate is using Euler's formula:

$$R = \left(\frac{\cos^2 \alpha}{M} + \frac{\sin^2 \alpha}{N} \right), \tag{4}$$

where M is the radius of curvature of the meridian section and N is the radius of curvature of the prime vertical section, and α is the azimuth from the grid node to the satellite. Notice that this atmospheric structure of type Eulerian normal spherical does *not* yield azimuthally symmetrical delays. Another way of computing the spherical radius is the Gaussian radius of curvature:

$$R = \sqrt{MN} \tag{5}$$

Only in this case the normal sphere is said to be an osculating sphere. Notice that although the radius is azimuth-independent it is still latitude-dependent. Yet another way of computing the radius of the normal sphere is as a constant, for all latitudes and azimuths, as is the case of the VMF1. Finally, in the limit of infinite radius, we obtain a flat-Earth or tangent plane atmospheric structure (Nievinski and Santos 2010).

The choice of radius of curvature can indeed cause a bias. Figure 7 shows three solutions spanning over latitude, for the original VMF1 and two UNB implementations, one using a constant radius, similar to the VMF, and one using Eq. (5). In this case, all UNB solutions use the CMC-GEM analysis. As a reference solution, full three-dimensional ray-tracing through the CMC-GEM was used (see Nievinski 2009 for more details). The use of a constant radius causes a 15-mm peak-to-peak variation in the slant delay (approx equal to ± 2 mm in station height) at the 5° elevation angle. Even with the Gaussian radius (black line) there is still a small latitude-dependent bias, but it is negligible in terms of error in station height.

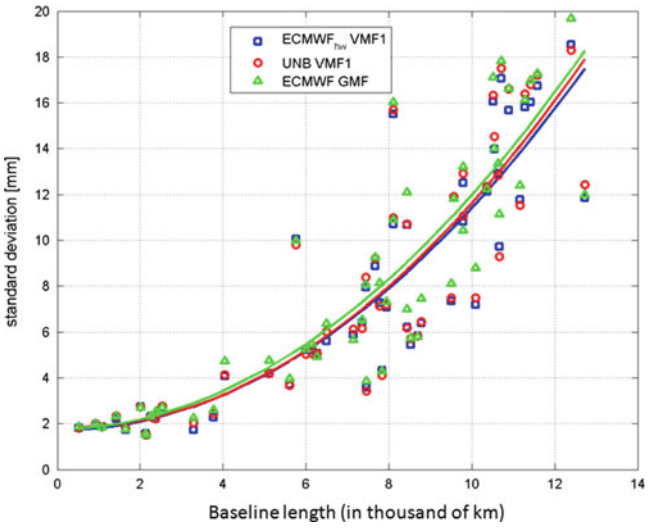

Fig. 8 Non-hydrostatic station height difference (ECMWF − NCEP). Values in mm

4.4 VLBI Results

Three solutions were used to process CONT08 (Teke et al. 2011) VLBI data sets: GMF (using a priori zenith delays derived from the ECMWF), VMF1 (using ECMWF), and UNB-VMF1 (using NCEP data). Gridded data was used. Results for baseline repeatability are shown in Fig. 8. Both VMF1's show improvement over the GMF, especially for longer baselines. The ECMWF VMF1 has the best performance overall. This may be due to the larger noise seen in the UNB a priori zenith delays. GMF repeatability worsens with baseline length; UNB-VMF1 follows VMF1 very well except for the very long baselines.

5 Concluding Remarks

Numerical weather models will continue to improve. As they do, they will become more useful for geodetic purposes. We have been generating VMF1-type grids using NCEP and GEM models at UNB. This is an attempt to satisfy consistency and redundancy issues.

Tests reported in this paper show that (a) zenith delays differences between VMF1 using ECMWF and NCEP are equal to -2.4 ± 3.8 mm for the hydrostatic, and -6.3 ± 14.7 mm for the non-hydrostatic components; (b) comparison to Saastamoinen showed a 2 mm (bias) and a 4 mm (st. dev.) and indicated that our use of NCEP was noisier than GEM; (c) difference in station height between ECMWF and NCEP showed a 0.8 ± 0.9 mm for the hydrostatic and -0.4 ± 0.6 mm for the non-hydrostatic components; (d) the impact of different radius of curvature was investigated, showing a latitude-dependent $\pm$ 2-mm height difference, largest at the poles and the equator; and finally, (e) impact on baseline repeatability using VLBI CONT08 data sets showed that the solutions using VMF1 and UNB-VMF1 are closer together than GMF, which got higher values.

As the UNB-VMF1 implementation gets developed in the future months, more tests are planned, including comparisons in the position domain using GPS campaigns and a look at effect on mean station position.

The future provision of UNB-VMF1 to the public will be similar to the current VMF1 service and will act as a backup or alternative for users.

Acknowledgments The authors acknowledge Matthias Madzak (TU Vienna) for processing the VLBI results, the weather agencies (ECMWF, NCEP and CMC) for providing access to the NWM data, and Natural Sciences and Engineering Research Council of Canada (NSERC) and the Austrian Science Fund (FWF, project P20902) for funding the research. Dow et al. 2009 is kindly acknowledged for the IGS products

References

Boehm J, van Dam T (2009) Modeling deficiencies and modeling based on external data. In: Second GGOS unified analysis workshop, IERS, Grand Hyatt, 11–12 December (oral presentation)

Boehm J, Niell AE, Tregoning P, Schuh H (2006a) Global Mapping Function (GMF): a new empirical mapping function based on numerical weather model data. Geophys Res Lett 33:L07304. doi:10.1029/2005GL025546

Boehm J, Werl B, Schuh H (2006b) Troposphere mapping functions for GPS and very long baseline interferometry from European Centre for medium-range weather forecasts operational analysis data. J Geophys Res 111:B02406. doi:10.1029/2005JB003629

Boehm J, Kouba J, Schuh H (2008) Forecast Vienna mapping functions 1 for realtime analysis of space geodetic observations. J Geodesy 83(5):397–401. doi:10.1007/s00190-008-0216-y

Dow JM, Neilan RE, Rizos C (2009) The international GNSS Service in a changing landscape of global navigation satellite systems. J Geodesy 83:191–198. doi:10.1007/s00190-008-0300-3

Fund F, Morel L, Mocquet A (2009) Discussion and recommendations about the height correction for a priori zenith hydrostatic delays derived from ECMWF data [on-line]. www.hg.tuwien.ac.at/~ecmwf1/Reducing_ECMWF_ZHDs.pdf

Herring TA (1992) Modelling atmospheric delays in the analysis of space geodetic data. In: de Munck JC, Th Spoelstra TA (eds) Proceedings of the symposium refraction of transatmospheric signals in Geodesy, No. 36, Netherlands Geodetic Commission, The Hague, 19–22 May, pp. 157–164

Kouba J (2008) Implementation and testing of the gridded Vienna Mapping Function 1 (VMF1). J Geodesy 82(4):193–205. doi:10.1007/s00190-007-0170-0

Marini JW (1972) Correction of satellite tracking data for an arbitrary tropospheric profile. Radio Sci 7(2):223–231. doi:10.1029/RS007i002p00223

Niell AE (1996) Global mapping functions for the atmosphere delay at radio wavelengths. J Geophys Res 101(B2):3227–3246. doi:10.1029/95JB03048

Nievinski FG (2009) Ray-tracing options to mitigate the neutral atmosphere delay in GPS. M.Sc.E. Thesis, Department of Geodesy and Geomatics Engineering technical report no. 262, University of New Brunswick, Fredericton, New Brunswick, 232 pp

Nievinski FG, Santos MC (2010) Ray-tracing options to mitigate the neutral atmosphere delay in GPS. Geomatica 64(2):191–207

Petit G, Luzum B (eds) (2010) IERS conventions (2010) (IERS technical note; 36). Verlag des Bundesamts für Kartographie und Geodäsie, Frankfurt am Main, 179 pp

Saastamoinen J (1972) Atmospheric correction for the troposphere and stratosphere in radio ranging of satellites. In: Henriksen SW, Mancini A, Chovitz BH (eds) The use of artificial satellites for Geodesy, vol. 15 of Geophysical monograph series. American Geophysical Union, Washington, DC, pp 247–251. ISBN 0-87590-015-1

Teke K, Böhm J, Nilsson T, Schuh H, Steigenberger P, Dach R, Heinkelmann R, Willis P, Haas R, García-Espada S, Hobiger T, Ichikawa R, Shimizu S (2011) Multi-technique comparison of troposphere zenith delays and gradients during CONT08. J Geodesy 85(7):395–413. doi:10.1007/s00190-010-0434-y

Tesmer V, Boehm J, Heinkelmann R, Schuh H (2007) Effect of different tropospheric mapping functions on the TRF, CRF and position time-series estimated from VLBI. J Geodesy 81:409–421. doi:10.1007/s00190-006-0126-9

Urquhart L (2010) Assessment of tropospheric slant factor models: comparison with three dimensional ray-tracing and impact of geodetic positioning. M.Sc.E thesis, Dept of Geodesy and geomatics Engineering technical report 275, University of New Brunswick, Fredericton, 166 pp

DORIS Tropospheric Estimation at IGN: Current Strategies, GPS Intercomparisons and Perspectives

Pascal Willis, Olivier Bock, and Yoaz E. Bar-Sever

Abstract

We reprocessed DORIS for all of 2010, using the latest model and strategy improvements to estimate Zenith Tropospheric Delays (ZTDs), as well as tropospheric horizontal gradients for about 60 ground stations. These results were compared to recent GPS-based estimates obtained at the Jet Propulsion Laboratory (JPL). After discussing some of the data processing options and current limitations of the DORIS data, we show that the DORIS-GPS comparisons possess a high degree of correlation (average being 0.97), and that total zenith delay estimates from the two techniques agree at the 3 mm level on average with 8.6 mm total RMS, with better results being obtained when a 5° elevation cutoff angle is used for DORIS. While these DORIS results cannot be used for real-time weather prediction, they could contribute to scientific investigations for climatology, thanks to the homogenous tracking network of the DORIS system, as well as the long-term history of the observation time series.

Keywords

DORIS • GPS • Horizontal tropospheric gradients • Zenith tropospheric delay

1 Introduction

While DORIS data have been used for years for Precise Orbit Determination (POD, Cerri et al. 2010; Lemoine et al. 2010) and Geodesy, only a few groups have tried to generate sufficiently long time series of DORIS tropospheric estimation (Willis et al. 2007a; Stepanek et al. 2010). These results were compared either during intensive campaigns such as CONT05 (Snadjrova et al. 2006) or CONT08 (Teke et al. 2011), showing small but regular improvements in data processing, or for long period of times (Bock et al. 2010), looking for possible biases relative to GPS estimation. More recently, additional parameters, such horizontal gradients (Bar-Sever et al. 1998), were derived when using the DORIS data (Flouzat et al. 2009; Willis et al. 2012) and compared to GPS estimations during a limited period of time. The goal of this paper is to present the latest tropospheric results obtained at the Institut national de l'information géographique et forestière (IGN, France) and to discuss their current accuracy, using direct comparisons with GPS data at most co-located sites in 2010.

We will first present some key aspects of the DORIS system and show how these observations can contribute to atmospheric sciences and climatology, but not yet to weather prediction (see discussion after). We will then describe our strategy to obtain zenith tropospheric delays and horizontal

P. Willis (✉)
Institut national de l'information Géographique et forestière (IGN), Direction Technique, 2 avenue Pasteur, 94165 Saint-Mandé, France

Institut de Physique du Globe de Paris, PRES Sorbonne Paris Cité, 35 rue Hélène Brion, 75013 Paris, France
e-mail: willis@ipgp.fr

O. Bock
Institut national de l'information Géographique et forestière (IGN), LAREG, 6-8 avenue Blaise Pascal, 77455 Marne-la-Vallée, France

Y.E. Bar-Sever
Jet Propulsion Laboratory, California Institute of Technology, 4800 Oak Grove Dr., Pasadena, CA, 91109 USA

C. Rizos and P. Willis (eds.), *Earth on the Edge: Science for a Sustainable Planet*, International Association of Geodesy Symposia 139, DOI 10.1007/978-3-642-37222-3_2,

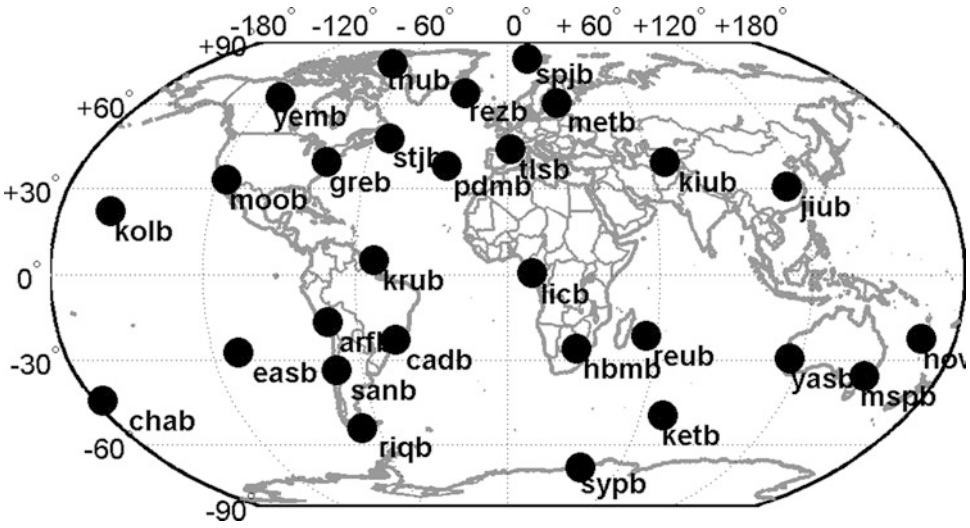

Fig. 1 DORIS/GPS co-located stations in 2010 selected in this study (acronyms correspond to DORIS stations).

tropospheric gradients using DORIS and GPS techniques. After describing the method used, we will discuss the results of our inter-comparisons.

2 DORIS Data

The DORIS system (Doppler Orbitography and Radiopositioning Integrated by Satellite) provides observations since the launch of the SPOT-2 satellite in 1990. However, best results are obtained after 1993, when two or more satellites are used (Williams and Willis 2006; Willis 2007). These data are easily accessible through data centers at IGN and at NASA/CDDIS (Noll 2010) through the International DORIS Service (IDS, Tavernier et al. 2002; Willis et al. 2010a).

This system is based on a permanent tracking network of about 60 beacons, transmitting radio-electrical signals at 2 GHz and 400 MHz from ground (uplink system). About half of these DORIS stations are co-located with other space geodesy equipment (VLBI, Satellite Laser Ranging, or GNSS). Figure 1 displays the 33 co-location sites that were used in this study, where the DORIS antenna is sufficiently close to the GPS antenna (less than 200 m difference in height).

It is important to notice that unlike GPS receivers, there are only two types of DORIS ground antennas: Alcatel and Starec. The Starec antennas have progressively replaced the Alcatel antennas, and now operate at all sites (Fagard 2006). As POD is the major application of the DORIS system, ground tracking stations were very rarely moved, allowing continuity of observation over long periods of time and consequently making DORIS results valuable for global monitoring (Altamimi et al. 2005; Nocquet et al. 2006; Willis et al. 2006; Argus et al. 2010). Until now very few studies investigated possible phase center offsets for DORIS antennas and none were yet able to demonstrate any significant error from the manufacturer specifications (Willis et al. 2005b, 2007b).

We restricted our study to 1 year and selected 2010, as 5 DORIS satellites could be used: SPOT-4, SPOT-5, Envisat, Jason-2, all observed during the full year, and Cryosat-2 for half a year (only after May 30, 2010). DORIS data from the Jason-1 satellite were disregarded, due to a large sensitivity to radiation of the onboard clock when crossing the South Atlantic Anomaly (SAA), as discussed in Willis et al. (2004), even after removing a correction model developed by Lemoine and Capdeville (2006).

Compared to GPS, there are two important differences for the DORIS data: first of all, these data are only available to users after about 4 weeks, making these data totally useless for real-time applications such as weather prediction. Unlike GPS, DORIS does not possess a constellation of satellites as such. The number of available DORIS satellites fluctuates with time (from 2 in 1993 up to 6 as of mid 2011) and is far less numerous than GNSS. Furthermore, the DORIS satellites usually orbit at lower altitude (800 and 1,300 km), while GNSS satellites orbit at much higher orbits (around 20,000 km). Consequently, the DORIS tracking stations do not provide continuous observations of several satellites simultaneously, but only a few data points during satellite passes. Simultaneous DORIS observations from two satellites from the same ground tracking site are rare events. Figure 2 provides an estimation of the total observation time per day (using one or more DORIS satellites) for two specific days: July 14, 2007 and July 14, 2010.

Figure 2 shows that the DORIS stations are only observed 7–15 % in 2007, but 15–35 % in 2010. This significant increase can be attributed to the two more recent satellites (Jason-2 and Cryosat-2, launched respectively on June 15, 2008 and April 8, 2010). Thanks to their new multi-channel technology, the DG-XX digital receivers onboard these satellites provide a larger amount of data thanks to the seven

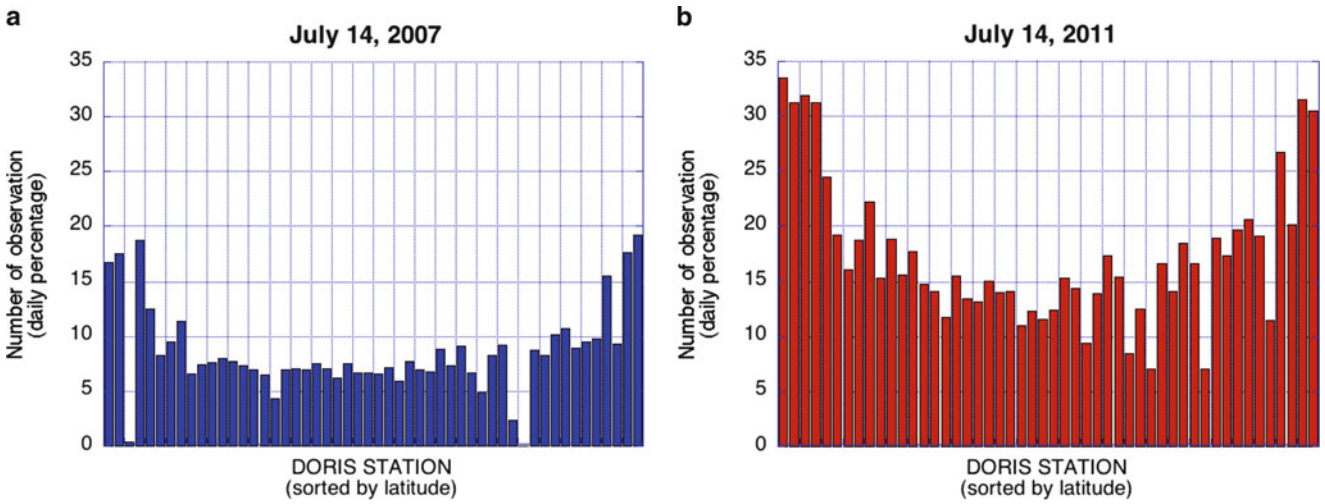

Fig. 2 Daily percentage of DORIS observation time available by station, sorted by latitude. As for (**a**) July 14, 2007 (*left*) and (**b**) July 14, 2010 (*right*)

parallels channels, especially for satellite observations at low elevation (Auriol and Tourain 2010). More observations are also available for higher latitude stations, due to the DORIS sun-synchronous (almost polar) satellites (Williams and Willis 2006).

For this study, we reprocessed the 2010 DORIS data, adopting a multi-satellite approach and making full use of the latest improvements in DORIS data processing at IGN using the GIPSY/OASIS software package (Willis et al. 2010b). In particular: resubmitted Jason-2 and Cryosat-2 data were used (DORISMail #0770); atmospheric drag parameter was estimated once per hour for the lowest satellites around 800 km, during geomagnetic storms and outside (Willis et al. 2005a; Gobinddass et al. 2010); solar radiation pressure coefficient was held fixed to empirical values derived using long DORIS data spans (Gobinddass et al. 2009a, b); a problem only related to SPOT-5 data over the SAA (Stepanek et al. 2010) was mitigated by disregarding DORIS data from this satellite over South America. We also improved our processing strategy by fixing station coordinates to their proper value after displacement, instead of using the first "occupation" of this station. This is important for stations that were impacted by nearby Earthquakes, such as Arequipa (Perfettini et al. 2005), Fairbanks (Eberhart-Phillips et al. 2003), Santiago (Vigny et al. 2011). A detailed list of these rare events can be found in Willis et al. (2009).

DORIS data were processed on a daily basis, estimating all satellite orbits and clocks as well as tropospheric parameters for ground stations. Station coordinates were held fixed to our internal tf_110726a solution [positions and velocities derived using the full DORIS data set since 1993.0, and aligned to ITRF2008 (Altamimi et al. 2011)]. We only use ITRF2008 to estimate the best estimates of the 7-parameters for each weekly station coordinate solution. However, our DORIS solution contains all available DORIS data and is corrected for discontinuities that may have appeared after the computation of ITRF2008 (e.g. Santiago, which was affected by the large Chile Earthquake on 27-FEB-2010 of magnitude 8.8). More details about this procedure is described in Willis et al. (2010b).

Several days (43 out of 365) were rejected due to large residuals. This problem is now properly understood and will be corrected in future solutions. It corresponds to an improper parameterization due to an erroneous Fortran namelist for options. Several parameters (including clock and zenith tropospheric delays) were not properly reset at start of passes and were assumed to be constant over long period of time, exceeding by far the specification of the DORIS instruments (in particular, the oscillator stability).

For every DORIS station, a Wet Zenith Delay was estimated several times per day, while the Dry Zenith Delay was held fixed to an a priori value based on the altitude of the station using a simple formula. This simplified formula could introduce some bias in the ZTD estimation, as demonstrated by Tregoning and Herring (2006). Our current strategy could then be improved in future data processing by using the GPT model as a priori for the dry troposphere (Boehm et al. 2007). To avoid estimating parameters when no data is available, tropospheric delays were only estimated at the start of satellite passes (but not more frequently than every 20 min when multiple satellites are available) or every 20 min (for longer satellite passes). The tropospheric delay is assumed constant over 20 min. We should emphasize here that DORIS ZTDs are not estimated by satellite pass (as done by most other IDS Analysis Centers), as such parameter should, by definition, be station-dependent and not satellite-dependent. We used the hydrostatic and wet GMF mapping functions (Boehm et al. 2006). The DORIS ZTD estimates with formal uncertainties larger than 7 mm (usually related to lack of observations) were rejected before further use in

the inter-comparison exercise. Two parameters per day were also estimated (North and East) for horizontal tropospheric gradients to account for potential asymmetry in the lower atmosphere.

3 GPS Data

We used the IGS combined tropospheric solutions (Byun and Bar-Sever 2009), generated by JPL's GIPSY-OASIS software package in a Precise Point Positioning (PPP) mode (Zumberge et al. 1997). The GMF tropospheric mapping function was employed (Boehm et al. 2006), and the elevation cut-off angle was set to 7°. The three tropospheric parameters (1 Wet Zenith Delays and 2 horizontal gradients) were estimated at 5-min interval as random-walk parameters. Phase Center Variation (PCV) maps were used from IGS calibration model igs05.atx (Schmid et al. 2007), making results compatible de facto with ITRF2005 (Altamimi et al. 2007). It is noteworthy to mention that the production of the IGS combined tropospheric solutions recently transitioned to the United States Naval Observatory (USNO), using a different software package and estimating tropospheric parameters as a constant piece-wise linear parameter. Tests were carried out between JPL and USNO to verify the good agreement between these two types of GPS solutions.

From the hundreds of GPS stations in this reprocessed solution, we only selected the ones in co-location with the DORIS beacons. The 5-min sampled GPS ZTD series were first decimated to 15-min interval, without any smoothing. The GPS ZTD estimates were also selected based on their formal uncertainties, with a maximum acceptance threshold of 10 mm.

4 GPS/DORIS ZTD Inter-comparison Procedure

The method is the same as described by Bock et al. (2010). DORIS ZTD estimates were corrected for any difference in height between the DORIS and GPS antennas to provide equivalent estimates at the same altitude (10 m of difference in height corresponds on average to ∼2.3 mm in ZHD and ∼0.65 mm in ZWD). Both hydrostatic and wet components of the differential tropospheric delay were corrected using the Saastamoinen model (Saastamoinen 1973) applied to atmospheric parameters (pressure, temperature and humidity) extracted from ECMWF reanalysis (ERA-interim; Dee et al. 2011). The atmospheric parameters were bilinearly interpolated from the four nearest grid points. Station pairs with difference in heights larger than 200 m were discarded (e.g. mahb and SEY1). Among the data retained, the largest difference in heights was 145.5 m (between hbmb and HRAO).

In a first step, we searched for possible outliers by inspecting the GPS and DORIS ZTD time series and their differences for all co-location pairs. Figure 3 shows an example for the site at Greenbelt Maryland, USA.

Differences which deviate from the mean by more than three times the standard deviation are classified as outliers. For this station pair, 39 comparisons are thus rejected, which leaves at the end 3,624 comparisons with a mean difference in ZTD of 0.7 mm and a scatter (standard deviation of differences between GPS and DORIS ZTDs) of 7.3 mm. The mean formal error for the DORIS estimates is also given (4.0 mm), but the result suggest that formal errors are slightly underestimated. Based on other studies, the DORIS ZTD errors are believed to be somewhat larger than GPS ZTD errors (Snadjrova et al. 2006; Bock et al. 2007; 2010; Teke et al. 2011).

5 Comparing Zenith Tropospheric Delays

Figure 4 shows the average ZTD observed at the DORIS stations and the differences (mean and standard deviation) and the correlation coefficient with GPS ZTD estimates. The mean ZTD (Fig. 4a) reflects the combined effect of altitude of the site (through the hydrostatic component which is proportional to surface air pressure) and total column water vapor (TCWV). Hence, sites close to Equator have usually high ZTD because of high TCWV (e.g. krub and libc) and sites in mountainous areas have weak ZTD because of low surface pressure (e.g. arfb, monb, reub).

Figure 4b shows that at most sites the mean difference (DORIS − GPS) is very close to zero. Only some sites have large positive biases (easb, arfb, cadb, with bias > 10 mm) or negative bias (cidb, with bias < −5 mm). These sites are also among those where the correlation between DORIS and GPS estimates is the smallest (Fig. 4d). The standard deviations of the differences (Fig. 4c) show larger values in the tropical region. In this region, the DORIS errors are expected to be larger because there are fewer observations from the near-polar orbiting satellites and water vapor fluctuations are larger.

We can see in Fig. 4d that the linear correlation coefficient between GPS and DORIS is very high (always above 0.9 and 0.97 on average). Consistent with the results of Bock et al. (2010), the best agreement between DORIS and GPS is found in the higher northern latitudes. The worst results

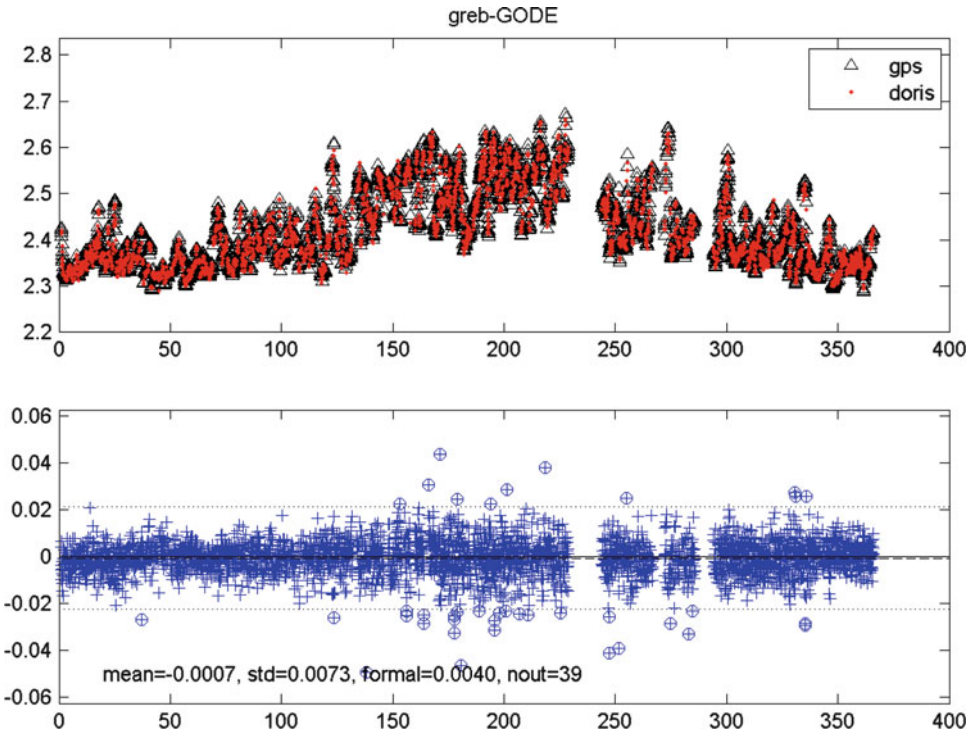

Fig. 3 *Upper plot*: example of ZTD estimates at Greenbelt site from DORIS (station greb) and GPS (station GODE) for year 2010. *Lower plot*: difference of ZTD estimates (DORIS − GPS). Unit are days of year (in 2010) for the *X*-axis and m for the *Y*-axis

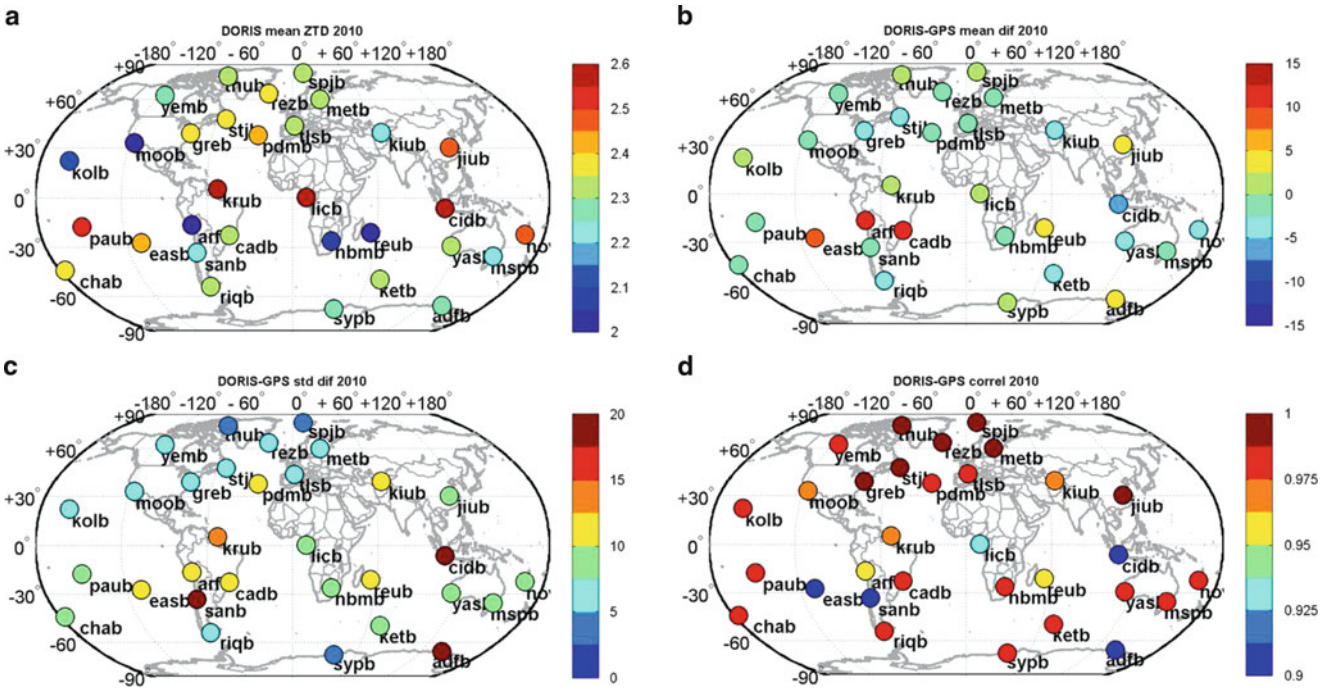

Fig. 4 (**a**) Mean ZTD from DORIS (unit m), (**b**) mean difference (DORIS ZTD minus GPS ZTD; unit mm), (**c**) standard deviation of difference (unit mm), (**d**) linear correlation coefficient, for the 41 sites observed in 2010. DORIS data were processed with a cutoff angle of 10° and estimation of a set of gradient parameters per day. Acronyms correspond to DORIS stations

Table 1 Overall ZTD statistics computed from the average over all sites, comparing different DORIS processing procedures

DORIS processing	Year	Median bias (m)	Mean ± one st. dev. of bias (m)	St. dev. diff. (m)	Correlation coefficient	No. sites
No gradient, 10°	2007	−0.0027	−0.0040 ± 0.0046	0.0079	0.979	40
1 gradient, 10°	2007	−0.0029	−0.0026 ± 0.0031	0.0086	0.973	40
1 gradient, 10°	2010	−0.0017	−0.0006 ± 0.0037	0.0086	0.969	45
1 gradient, 5°	2010	−0.0006	−0.0000 ± 0.0035	0.0086	0.969	45

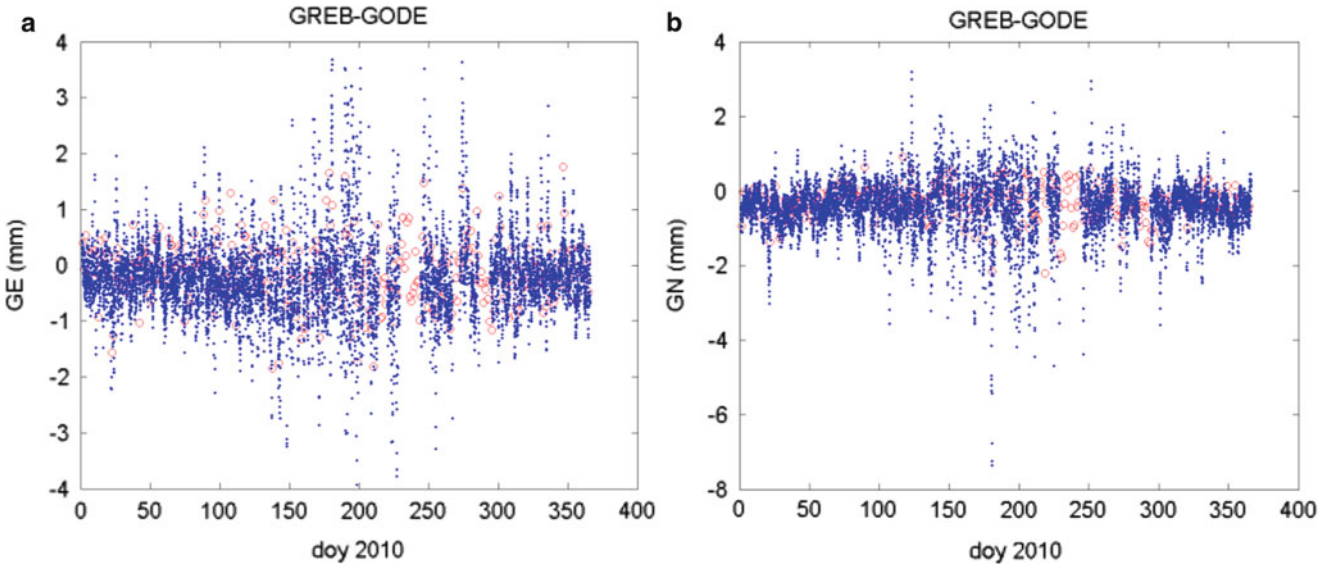

Fig. 5 (**a**) East–west gradient, (**b**) North–south gradient, DORIS station greb (in *red*) vs. GPS station GODE (in *blue*); DORIS processing procedure: 1 gradient/day, 5° cutoff; GPS processing procedure: 1 gradient/5 min (here averaged over 1 h), 7° cutoff

are seen the southern hemisphere at stations easb, sanb, cidb, adfb. Inspection of ZTD time series reveals that at stations cidb and adfb the outlier rejection was not efficient. Large errors remain in the DORIS solution which are not yet completely understood. Discarding these two stations, one can see that the stations where the correlation coefficient is smaller than 0.95 are all located in the southern hemisphere. The results shown in Fig. 4 differ slightly from those published by Bock et al. (2010).

The reason may be differences in DORIS and GPS data processing. Table 1 reports results for different DORIS processing procedures and different years. The first row for year 2007 is from Bock et al. (2010). The impact of estimating tropospheric gradients can be assessed by comparing the second row to the first row. The median is not affected, but both the mean bias and scatter in the bias over the ensemble of 40 stations decrease significantly. This indicates that estimating gradients improves the DORIS ZTD estimates, on average. The standard deviation of difference however increases slightly. This is expected because more parameters are estimated with the same amount of observations. The biases in 2010 (3rd and 4th row) are even smaller, demonstrating a nearly zero bias in ZTD between DORIS and GPS. Switching from a cutoff angle of 10–5° does slightly further reduce the bias.

6 Comparing Horizontal Tropospheric Gradients

In our DORIS and GPS data processing, horizontal gradients were also estimated to account for a possible asymmetry of the local troposphere. The estimated values are very small (rarely above 2 or 3 mm). Figure 5 shows an example for an important co-located site in Greenbelt.

In Fig. 5, the estimated values for GPS and DORIS are very small, showing larger scatter for both GPS and DORIS around July, probably related to the more humid and variable weather in the Washington DC area at this time of year. Correlation between GPS and DORIS horizontal gradients were already discussed in Willis et al. (2012). For the station in Greenbelt, the correlation between GPS and DORIS horizontal gradients is 0.40 in East and 0.46 in North. When taking in consideration all co-located sites, correlation between GPS and DORIS gradients is 0.267 in East and 0.370 in North.

7 Conclusions

In conclusion, ZTDs derived from a reprocessed DORIS data analysis in 2010 demonstrate only a minor improvement from previous solutions. Comparisons with IGS/ZTDs products show a high degree of correlation (0.97 on average) and demonstrate on average a 3 mm-level agreement (with 8.6 mm for RMS) between DORIS and GPS ZTDs results derived from the same software package (GIPSY-OASIS II) but using independent data and different data analysis strategies. Best comparisons are obtained when tropospheric gradients are estimated for DORIS and when a lower elevation cutoff (5°) is used. A complete reprocessing of the DORIS data since 1993.0 is now necessary in order to optimize the use these results for future climatic studies.

Acknowledgements Part of this work was supported by the Centre National d'Etudes Spatiales (CNES). Part of this work was carried out at the Jet Propulsion Laboratory, California Institute of Navigation, under a contract with the National Aeronautics and Space Administration. It is based on observations with DORIS embarked on SPOTs, TOPEX/Poseidon, Envisat, Jason-2 and Cryosat-2 satellites. This paper is IPGP contribution number 3286.

References

Altamimi Z, Boucher C, Willis P (2005) Terrestrial reference frame requirements within IGGOS, in IGGOS science rationale. J Geodyn 40(4–5):363–374

Altamimi Z, Collilieux X, Legrand J, Garayt B, Boucher C (2007) ITRF2005, a new release of the international terrestrial reference frame based on time series of station positions and earth orientation parameters. J Geophys Res 112(B9) (art. B09401)

Altamimi Z, Collilieux X, Métivier L (2011) ITRF2008, an improved solution of the international terrestrial reference frame. J Geod 85(8):457–473

Argus DF, Gordon RG, Heflin MB, Ma C, Eanes R, Willis P, Peltier WR, Owen S (2010) The angular velocities of the plates and the velocity of Earth's center from space geodesy. Geophys J Int 180(3):916–960

Auriol A, Tourain C (2010) DORIS system, the new age. Adv Space Res 46(12):1484–1496

Bar-Sever YE, Kroger PM, Borjesson JA (1998) Estimating horizontal gradients of tropospheric path delay with a single GPS receiver. J Geophys Res 103(B3):5019–5035

Bock O, Bouin MN, Walpersdorff A, Lafore JP, Janicot S, Guichard F, Agusti-Panadera A (2007) Comparison of ground-based GPS precipitable water vapour to independent observations and NWP model reanalyses over Africa. Quat J R Meteror Soc 133(629):2011–2027

Bock O, Willis P, Laccara M, Bosser P (2010) An inter-comparison of zenith tropospheric delays derived from DORIS and GPS data. Adv Space Res 46(12):1648–1660

Boehm J, Niell A, Tregoning P, Schuh H (2006) Global Mapping Function (GMF), a new empirical mapping function based on numerical weather model data. Geophys Res Lett 33(7)

Boehm J, Heinkelmann R, Schuh H (2007) A global model of pressure and temperature for geodetic applications. J Geod 81(10):679–683

Byun SH, Bar-Sever YE (2009) A new type of troposphere zenith path delay product of the International GNSS service. J Geod 83(3–4):367–373

Cerri L, Berthias JP, Bertiger WI, Haines BJ, Lemoine FG, Mercier F, Ries JC, Willis P, Zelensky NP, Ziebart M (2010) Precision orbit determination standards for the Jason series of altimeter missions. Mar Geod 33(S1):379–418

Dee DP, Uppala SM, Simmons AJ, Berrisford P, Poli P et al (2011) The ERA-interim reanalysis, configuration and performance of the data assimilation system. Quat J R Meteor Soc 137(656):553–597

Eberhart-Phillips D, Hauessler PJ, Freymueller JT, Frankel AD, Rubin CM et al (2003) The 2002 Denali fault earthquake, Alaka, a large magnitude, slip-partitioned event. Science 300(5622):1113–1118

Fagard H (2006) Twenty years of evolution for the DORIS permanent network, From its initial deployment to its renovation. J Geod 80(8–11):429–456

Flouzat M, Bettinelli P, Willis P, Avouac JP, Heriter T, Gautam U (2009) Investigating tropospheric effects and seasonal position variations in GPS and DORIS time series from the Nepal Himalaya. Geophys J Int 178(3):1246–1259

Gobinddass ML, Willis P, de Viron O, Sibthorpe AJ, Zelensky NP, Ries JC, Ferland R, Bar-Sever YE, Diament M (2009a) Systematic biases in DORIS-derived geocenter time series related to solar radiation pressure mis-modelling. J Geod 83(9):849–858

Gobinddass ML, Willis P, de Viron O, Sibthorpe A, Zelensky NP, Ries JC, Ferland R, Bar-sever YE, Diament M, Lemoine FG (2009b) Improving DORIS geocenter time series using an empirical rescaling of solar radiation pressure. Adv Space Res 44(11):1279–1287

Gobinddass ML, Willis P, Diament M, Menvielle M (2010) Refining DORIS atmospheric drag estimation in preparation of ITRF2008. Adv Space Res 46(12):1566–1577

Lemoine JM, Capdeville H (2006) A corrective model for Jason-1 DORIS Doppler data in relation of the South Atlantic anomaly. J Geod 80(8–11):507–523

Lemoine FG, Zelensky NP, Chinn D, Pavlis D, Beckley B, Lutchke SB, Willis P, Ziebart M, Sibthorpe A, Boy JP, Luceri V (2010) Towards development of a consistent orbit determination, TOPEX/Poseidon, Jason-1 and Jason-2. Adv Space Res 46(12):1513–1540

Nocquet JM, Willis P, Garcia S (2006) Plate kinematics in Africa and surrounding plates from a combination of DORIS and GPS solutions. J Geod 80(8–11):591–607

Noll CE (2010) The crustal dynamics data information system, a resource to support scientific analysis using space geodesy. Adv Space Res 45(12):1421–1440

Perfettini H, Avouac JP, Ruegg JC (2005) Geodetic displacements and aftershocks following the 2001 Mw = 8.4 Peru earthquake, implications for the mechanics of the earthquake cycle along subduction zones. J Geophys Res 110(B9)

Saastamoinen J (1973) Contribution to the theory of atmospheric réfraction. Bull Geod 107:1334

Schmid R, Steigenberger P, Gendt G, Ge M, Rothacher M (2007) Generation of a consistent absolute phase center correction model for GPS receiver and satellite antennas. J Geophys Res 81:781–798

Snadjrova K, Boehm J, Willis P, Haas R, Schuh H (2006) Multi-technique comparison of tropospheric zenith delays derived from CONT02 campaign. J Geod 79(10–11):613–623

Stepanek P, Dousa J, Filler V, Hugentobler U (2010) DORIS data analysis at GOP using single-satellite and multi-satellite solutions. Adv Space Res 46(12):1578–1592

Tavernier G, Soudarin L, Larson K, Noll C, Ries J, Willis P (2002) Current status of the DORIS pilot experiment and the future international DORIS service. Adv Space Res 30(2):151–156

Teke K, Böhm J, Nilsson T, Schuh H, Steigenberger P, Dach R, Heinkelmann R, Willis P, Haase R, Garcia-Espada S, Hobiger T,

Ichikawa R, Shimizu S (2011) Multi-technique comparison of troposphere zenith delays and gradients during CONT08. J Geod 85(7):395–413

Tregoning P, Herring TA (2006) Impact of a priori zenith hydrostatic delay errors on GPS estimates of station heights and zenith total delays. Geophys Res Lett 33(23), art. L23303

Vigny C, Socquet A, Peyrat S, Ruegg JC, Metois M, Madariaga R, Morvan S, Lancieri M, Lacassin R, Campos J, Carrizo D, Bejar-Pizarro M, Barrientos S, Armijo R, Aranda C, Valderas-Bermejo MC, Otrega I, Bondoux F, Baize S, Lyon-Caen H, Pavez A, Vilotte JP, Bevis M, Brooks B, Smalley R, Parra H, Baez JC, Nlanco M, Cimbaro S, Kendrick E (2011) The 2010 Mw 8.8 Maule megathrust earthquake of central Chile, monitored by GPS. Science 332(6036):1417–1421

Williams SDP, Willis P (2006) DORIS network, error analysis of weekly station coordinates. J Geod 80(8–11):525–539

Willis P (2007) Analysis of a possible future degradation in the DORIS geodetic results related to changes in the satellite constellation. Adv Space Res 39(10):1582–1588

Willis P, Haines B, Berthias JP, Sengenes P, Le Mouel JL (2004) Behavior of the DORIS/Jason oscillator over the South Atlantic anomaly. C R Geosci 336(9):839–846

Willis P, Deleflie F, Barlier F, Bar-Sever YE, Romans L (2005a) Effects of thermosphere total density perturbations on LEO orbits during severe geomagnetic conditions (Oct - Nov 2003). Adv Space Res 36(3):522–533

Willis P, Desai SD, Bertiger WI, Haines BJ, Auriol A (2005b) DORIS satellite antenna maps derived from long-term residuals time series. Adv Space Res 36(3):486–497

Willis P, Jayles C, Bar-Sever YE (2006) DORIS, from altimeric missions orbit determination to geodesy. C R Geosci 338(14–15):968–979

Willis P, Soudarin L, Jayles C, Rolland L (2007a) DORIS applications for solid earth and atmospheric sciences. C R Geosci 339(16):949–959

Willis P, Haines BJ, Kuang D (2007b) DORIS satellite phase center determination and consequences on the derived scale of the terrestrial reference frame. Adv Space Res 39(10):1589–1596

Willis P, Ries JC, Zelensky NP, Soudarin L, Fagard H, Pavlis EC, Lemoine FG (2009) DPOD2005, realization of a DORIS terrestrial reference frame for precise orbit determination. Adv Space Res 44(5):535–544

Willis P, Fagard H, Ferrage P, Lemoine FG, Noll CE, Noomen R, Otten M, Ries JC, Soudarin L, Tavernier G, Valette JJ (2010a) The international DORIS service, toward maturity. Adv Space Res 45(12):1408–1420

Willis P, Boucher C, Fagard H, Garayt B, Gobinddass ML (2010b) Contributions of the French Institut Géographique National (IGN) to the international DORIS service. Adv Space Res 45(12):1470–1480

Willis P, Bar-Sever YE, Bock O (2012) Estimating horizontal tropospheric gradients in DORIS data processing, preliminary results. IAG Symp 136:1011–1017

Zumberge JF, Heflin MB, Jefferson DC, Watkins MB, Web MH (1997) Precise point positioning for the efficient and robust analysis of GPS data from large networks. J Geophys Res 102(B3):5005–5017

The Australian Space Research Program Project: Platform Technologies for Space Atmosphere and Climate: Progress and Preliminary Results

K. Zhang, J. Sang, C.S. Wang, J.C. Bennett, B. Carter, R. Norman, and S. Wu

Abstract

This paper introduces the multi-million-dollar Australian Space Research Program (ASRP) Project—"Platform Technologies for Space Atmosphere and Climate," recently awarded to an international consortium led by RMIT University, and reports the current progress and some results achieved so far. The project is part of the Australian Government's recent space-related initiatives to support national strategic, economic and social objectives. Its main focus is developing new algorithms, new approaches, and software and system platforms for enhancing Australia's capability in space-related research and promoting innovative applications of space-related cutting-edge technologies in Australia. The aim and objectives, major research tasks, anticipated outcomes and key issues related to Australian space research and space industry are outlined and the progresses recently made and some selected key results are reported.

Keywords

Atmospheric modelling • GPS RO • Ray-tracing • Space tracking

1 Introduction

Geodesy is the science of measuring the size and shape of the Earth, and the Global Navigation Satellite Systems (GNSS) as a vital locationing technology have become a critical space-based infrastructure widely used for both geodesy and space research. Geodesy and GNSS together play a critical role in many aspects of space research. This includes, but is not limited to: (1) precise orbit determination (POD) of space objects; (2) precise positioning using space geodesy techniques, such as GNSS, Satellite Laser Ranging (SLR) and Very Long Baseline Interferometry (VLBI) techniques; and (3) atmosphere modeling for positioning, space weather, space tracking and climatology. These research areas have made, and will continue to make, significant contributions to space-related applications, e.g. space situational awareness, the tracking and navigation of space objects, the surveillance and orbit prediction of space debris for space safety, and the monitoring of space weather and climate change.

To keep abreast of advanced international research and to play a leading role in the space-related research arena, the SPACE Research Centre at RMIT University, in collaboration with its international partners, took an initiative in mid-2010 to embark on this research. The 3-year, $7.5 million Platform Technologies project is supported by the ASRP through a competitive process. The international consortium consists of RMIT University, the University of New South Wales, Curtin University of Technology, Bureau of Meteorology, Electro Optic Systems Space System, GPSat Systems Australia, and National Central University, Taiwan with support from the National Space Organisation of Taiwan and the World Data Center for Meteorology from USA. The consortium is a typical mixture of government, academia, research organisations and industry.

K. Zhang (✉) • J. Sang • C.S. Wang • J.C. Bennett • B. Carter • R. Norman • S. Wu
SPACE Research Centre, School of Mathematical and Geospatial Sciences, RMIT University, GPO Box 2476, Melbourne, VIC, Australia
e-mail: kefei.zhang@rmit.edu.au

C. Rizos and P. Willis (eds.), *Earth on the Edge: Science for a Sustainable Planet*, International Association of Geodesy Symposia 139, DOI 10.1007/978-3-642-37222-3_3,

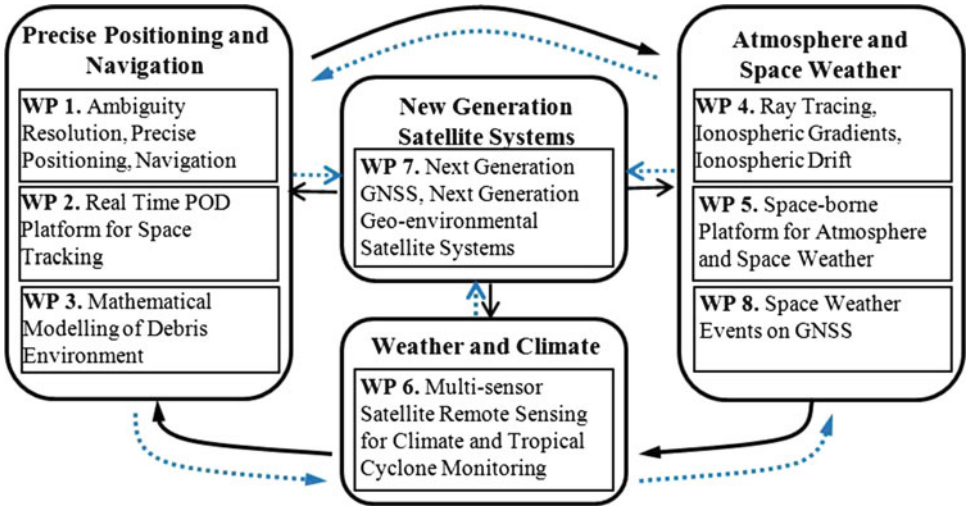

Fig. 1 The four key research themes and their associated eight work packages, and the road map displaying their relationships

2 Aim and Objectives

The aim of this project is to enhance Australia's space capabilities by developing integrated and advanced space-based platform technologies through a multi-sensor satellite remote sensing approach. Theoretical, technical and practical application issues related to new generation navigation and geo-environmental remote sensing satellite systems will be investigated, assessed and addressed along with the benefits and challenges. The key objectives of this project are:

- To develop advanced algorithms for precise real-time or near real-time in-space tracking and navigation, and POD for current and future geo-environmental satellites;
- To investigate atmospheric mass density models for improving the accuracy and reliability of orbit determination of space objects and space surveillance systems;
- To develop new algorithms and optimisation for precise ubiquitous positioning and mapping in the context of new generation GNSS;
- To investigate the effects of the Earth's magnetic field, the troposphere, the stratosphere and the ionosphere on the electro-magnetic L-band frequency ray paths by developing comprehensive 3D ray tracing application software packages;
- To study the atmosphere, the ionosphere and space weather using GNSS and the low Earth orbit (LEO) radio occultation (RO) technique;
- To evaluate and assimilate remote sensing data from multi-sensor satellites for investigating climate change and climatic hazards; and
- To improve the characterisation of climate in the Australian region based on the new models and methodologies developed.

Apart from these, with the advent of next generation GNSS, new models and algorithms for incorporating multi-GNSS multi-frequency observations, the exploration of next generation GNSS and new geo-environmental satellite programs (e.g. COSMIC II) will be also investigated for addressing the issues Australia faces, e.g. climate change and natural disasters including tropical cyclones, drought, extreme heat and bushfires. Due to the insufficient density of ground-based meteorological stations in the southern hemisphere and the lack of meteorological observations over the world's oceans and polar regions, it is also proposed to explore the acquisition, processing and analysis of more observation data, especially data from multi-sensor satellite remote sensing to be offered by the new geo-environmental satellites particularly in the Australian context.

3 Research Roadmap

This project covers four main research themes categorised into eight working packages (WPs). The relationship among these four main areas and associated eight WPs as well as the specific research topics in each WP are shown in Fig. 1.

4 Research Results to Date

Research in the aforementioned areas has been conducted and substantial progress has been made (e.g. Bennett and Sang 2011; Le Marshall et al. 2010, 2012; Norman et al. 2012a, 2013; Pavelyev et al. 2012; Sang et al. 2011, 2012; Zhang et al. 2010, 2011). Of these results, four recently achieved in selected areas are briefly reported below.

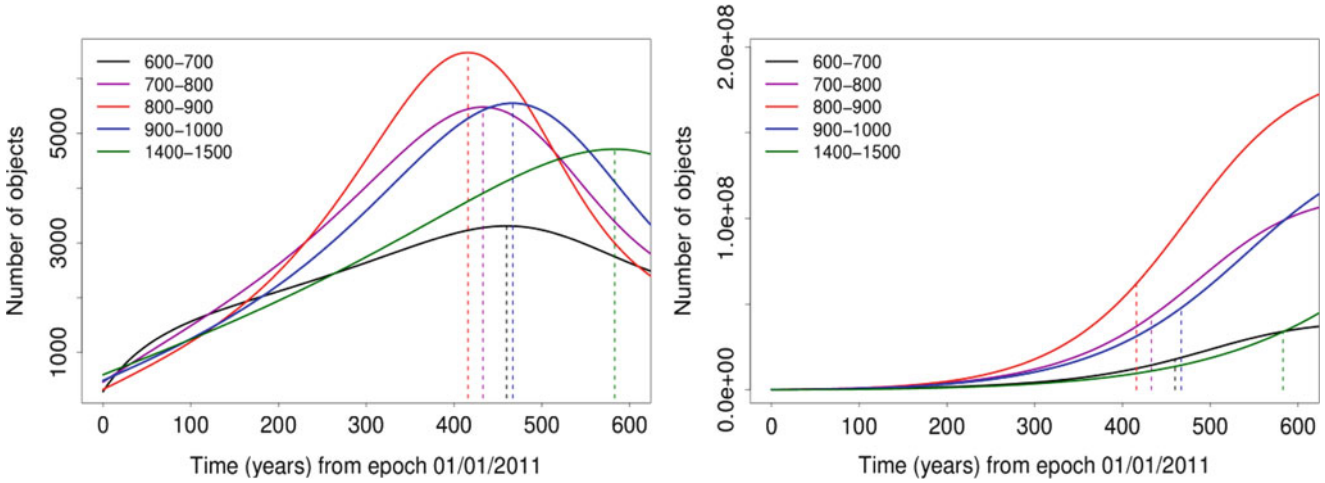

Fig. 2 Plot of long term evolution of objects with mass ≥ 80 kg (*left*) and ≤ 0.5 kg (*right*) for the altitude shells (in km) with the greatest spatial density (from Bennett and Sang 2011)

4.1 Mathematical Modelling of the Low-Earth Orbit Environment

Orbital debris present in the LEO environment poses a threat to the success of future space operations. On 10 February 2009 the inactive Russian communications satellite, Cosmos 2251, collided with an active US communications satellite, Iridium 33, at an altitude of 789 km. This has led to thousands of debris fragments larger than 1 cm in diameter. This event highlighted the increasing threat that space debris has to space operations.

Simulation models assessing the change in debris population have been developed since Kessler and Cour-Palais (1978) first predicted the onset of collisional cascading (the Kessler Syndrome). Our initial model, although simpler than some of the models in the literature, represents a platform to extend in future analyses towards a comprehensive evolutionary model with the ability to investigate a variety of mitigation and active debris removal studies. A nonlinear source-sink model is developed to analyse the evolution of the LEO debris. The change in population in altitudinal shells spanning the range between 200 and 2,000 km can be estimated using this model. The model contains terms that simulate launches, the release of launch-related debris, explosions, decay due to atmospheric drag and collisions. The parameters driving the model were estimated using recent observations of space operations as well as information present in the literature. The model is flexible and details may be found in Bennett and Sang (2011). Figure 2 shows the results of the model run over a simulation time span of 600 years for the altitudinal ranges with the greatest spatial density.

The key feature to notice is the population of large objects reaches a level after which there is a large reduction. This is a result of the collisional cascading effect where the probability of a collision increases to a level where debris created from collisions dominates the environment. The populations of small objects increase exponentially before tending towards equilibria.

Further refinements are currently under development to extend the model to simulate a wide range of mitigation and active debris removal studies. The focus of the research will be on creating improved approximations for the atmospheric decay as well as introducing an orbit propagator with the capability of rapid orbit predictions to improve the predictive capability of the model.

4.2 Investigation of Atmospheric Parameters Over Australia Using GPS RO Technique

The long-term stability, high accuracy, all-weather capability, high vertical resolution and global coverage of the GPS RO technique make it important for monitoring global atmospheric temperature changes (Kursinski et al. 1997; Leroy and North 2000; Hajj et al. 2002). This technique has shown that it could be used to significantly improve weather forecasting in the Australian region (Le Marshall et al. 2010, 2012). COSMIC (Anthes et al. 2008) is the first GPS RO mission developed by Taiwan's National Space Organization (NSPO) and the University Corporation for Atmospheric Research (UCAR) in collaboration with NASA. The COSMIC Data Analysis and Archive Center (CDAAC) from

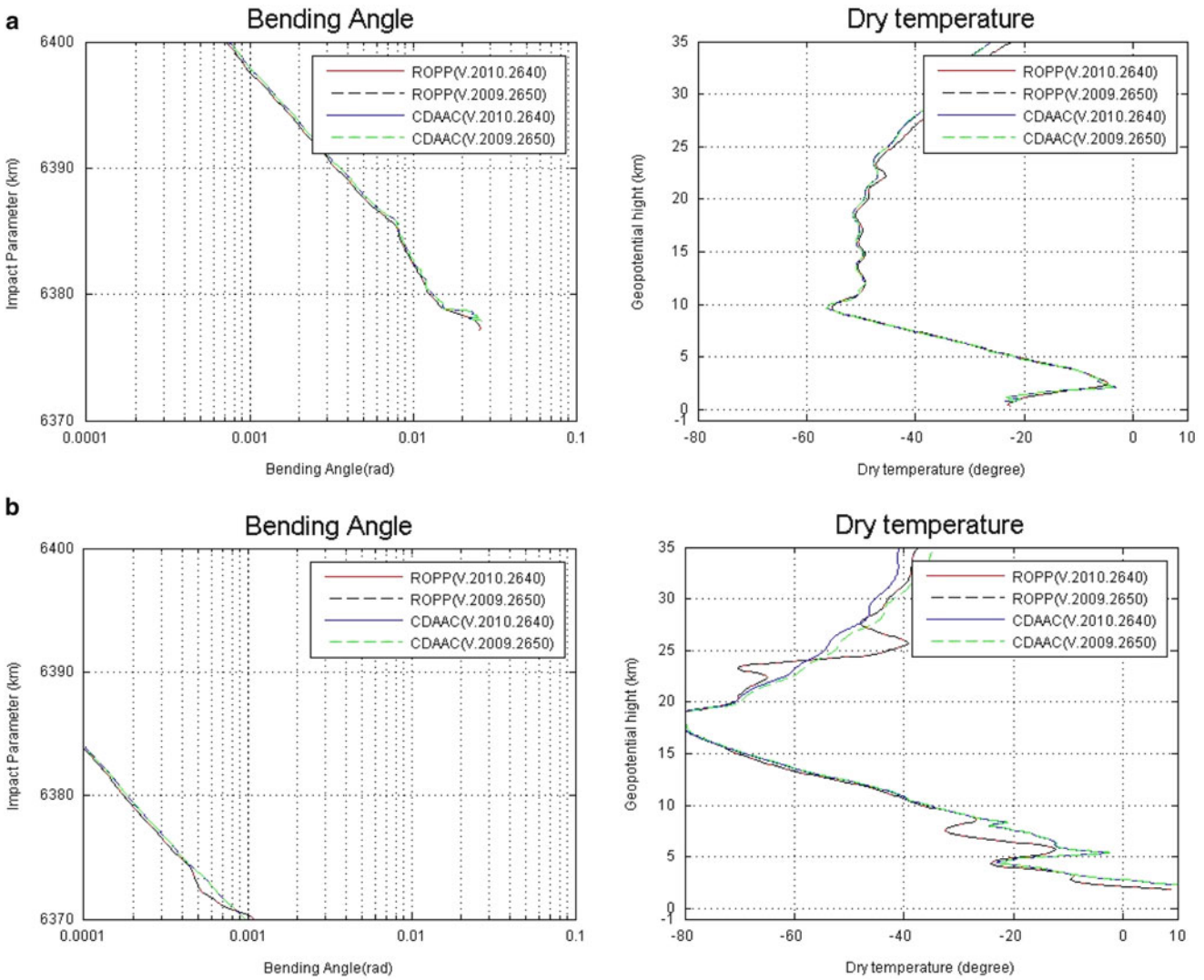

Fig. 3 Retrieved atmospheric profiles from ROPP and CDAAC (V2009.2650 and V2010.2640) for Event1 and Event2 respectively. (**a**) Radio occultation event 1 (Event1). (**b**) Radio occultation event 2 (Event2)

UCAR provides near real-time measurements as well as post-processed and derivative products of the atmosphere. The latest products are version 2010.2640 (V.2010.2640), produced by CDAAC 3.0 and launched in February, 2011 and its previous product is version 2009.2650 (V.2009.2650) created by CDAAC 2.0 in 2010.

The RO Processing Package (ROPP) is a software package developed for the GRAS (Global Navigation Satellite System Receiver for Atmospheric Sounding) SAF (Satellite Application Facilities) project led by the Danish Meteorological Institute (DMI) for processing RO data from MetOp satellites. Its version V4.1 was used in this research for comparisons of atmospheric results from COSMIC observations over the Australian region using both ROPP and CDAAC (the aforementioned two versions of CDAAC products, i.e. V.2009.2650 and V.2010.2640 were all used). The test results for bending angle and dry temperature are shown in Fig. 3.

From the dry temperature profiles obtained from the two software packages, it can be seen that, the largest differences are 2.51° and 5.53° for Event 1 (25–35 km altitude) and Event 2 (5–10 km altitude) respectively. The smallest differences for both events are at the altitudes of 10–20 km. The average differences at the altitudes of 5–35 km are in the range of 0–3.5°. Moreover, the average differences resulted from the two CDAAC versions approach 1.6° and 0.9° at the altitudes of 25–35 km and 5–10 km respectively.

For the bending angle, Fig. 3 shows an insignificant and consistent offset caused by the two versions of the two software packages. In addition, tests for refractivity and pressure were also performed and results show no significant

differences caused by either the two software packages or the two versions of each package.

4.3 Numerical and Analytical Ray-Tracing Algorithms and Software for Determining Satellite-to-Satellite L-Band Radio Frequency Paths

Ray tracing techniques are commonly used for calculating the path of an electromagnetic signal in a medium specified by a refractive index. The numerical method and closed form or analytic methods are often used in ionospheric ray tracing. A new 3-D numerical ray tube technique has been developed in this research (Norman et al. 2012b, 2013). It uses eighteen differential equations representing the position and direction of the principle ray path as well as the two linearly independent variational ray paths, and these equations are integrated simultaneously at each point along the ray path, to determine ray parameters such as the group path, phase path, angle of arrival and signal strength. The program has a homing-in algorithm capable of determining the correct part of the signal reaching the LEO satellite.

A new pseudo technique called 3-D Segment Method Analytical ray Tracing Technique (3D SMART) has also been developed (Norman et al. 2012a). Analytic ray tracing techniques use explicit equations to define the ionosphere and to determine the ray path and ray parameters. Thus this technique is computationally much powerful than numerical ray tracing but it is normally restricted to simple spherically stratified ionospheric models. This new 3-D SMART technique approximates the down range horizontal and transverse electron density gradients by automatically segmenting the ionosphere in the direction of the ray path and has the ability to trace the ray through complicated ionospheric models such as IRI2007.

4.4 The Effects of Space Weather on GPS Signals

The COSMIC RO data has been also used to investigate the effects of the space environment, in particular the F-region plasma irregularities on the GPS signals (Carter et al. 2013). The global coverage of the COSMIC RO data allows a detailed characterisation of the F-region irregularities that can be used to study the environmental factors that cause amplitude and phase scintillations on the GPS signals.

The COSMIC data collected during 2007–2010 were used to investigate the spatial and temporal extent of the equatorial F-region irregularities. In addition to measuring the ionospheric electron density profile for each RO event, the COSMIC satellites also recorded the signal-to-noise fluctuations of the 50-Hz L1 measurements, which were then used to calculate a proxy for the S4 amplitude scintillation index (Ko and Yeh 2010). The parameter used in this work is the "s4max9s," which is the average of the S4 values corresponding to the 9-s period surrounding the time the maximum S4 value was measured for the RO event. Values of s4max9s ≥ 0.3 are indicative of F-region irregularities when detected at tangent-point altitudes above 150 km.

Figure 4 shows the occurrence of F-region irregularities in terms of their latitudinal and local-time (LT) distributions for different longitude sectors (columns) and seasons (rows) during low geomagnetic activity periods (i.e. Kp ≤ 3). It is clear that the irregularities are mostly detected in the post-sunset time sector within 50° dip latitude of the magnetic equator. However, the exact dip latitude-LT distribution is significantly different depending on the time of year and the longitude sector considered. These climatological features quite closely match that reported previously; e.g. the results of equatorial plasma bubble occurrence using in situ satellite observations by Burke et al. (2004). As explained by Tsunoda (1985), the primary reason for the variations shown between the panels in Fig. 4 is the difference in the magnitude of the zonal gradients in the flux-tube integrated E-region conductivity at different times of the year and in different longitude sectors. During periods when the day-night terminator closely aligns with the direction of the Earth's magnetic field, the longitudinal conductivity gradient is large, which results in a stronger post-sunset upward plasma drift that gives rise to F-region plasma bubbles and irregularities.

The large dataset employed in this work also has the potential to be used to investigate the effects of geomagnetic disturbances on the equatorial F-region irregularity occurrence and their spatio-temporal distribution, which will significantly augment current space weather forecasting capabilities for the use of GPS-reliant applications.

5 Summary and Concluding Remarks

This paper introduced the 3-year, $7.5 Platform Technologies project awarded to a consortium led by SPACE Research Centre at RMIT University under the Australian government recent initiative of ASRP. The potential of space research in the broad picture of advanced space geodesy techniques is shown. It is expected that this research will have a significant and profound impact on efficient and effective uses of space geodesy techniques for space tracking, precise satellite positioning, atmosphere and climate monitoring etc., especially in the Australian context. A variety of research tasks and substantial results achieved so far have shown very

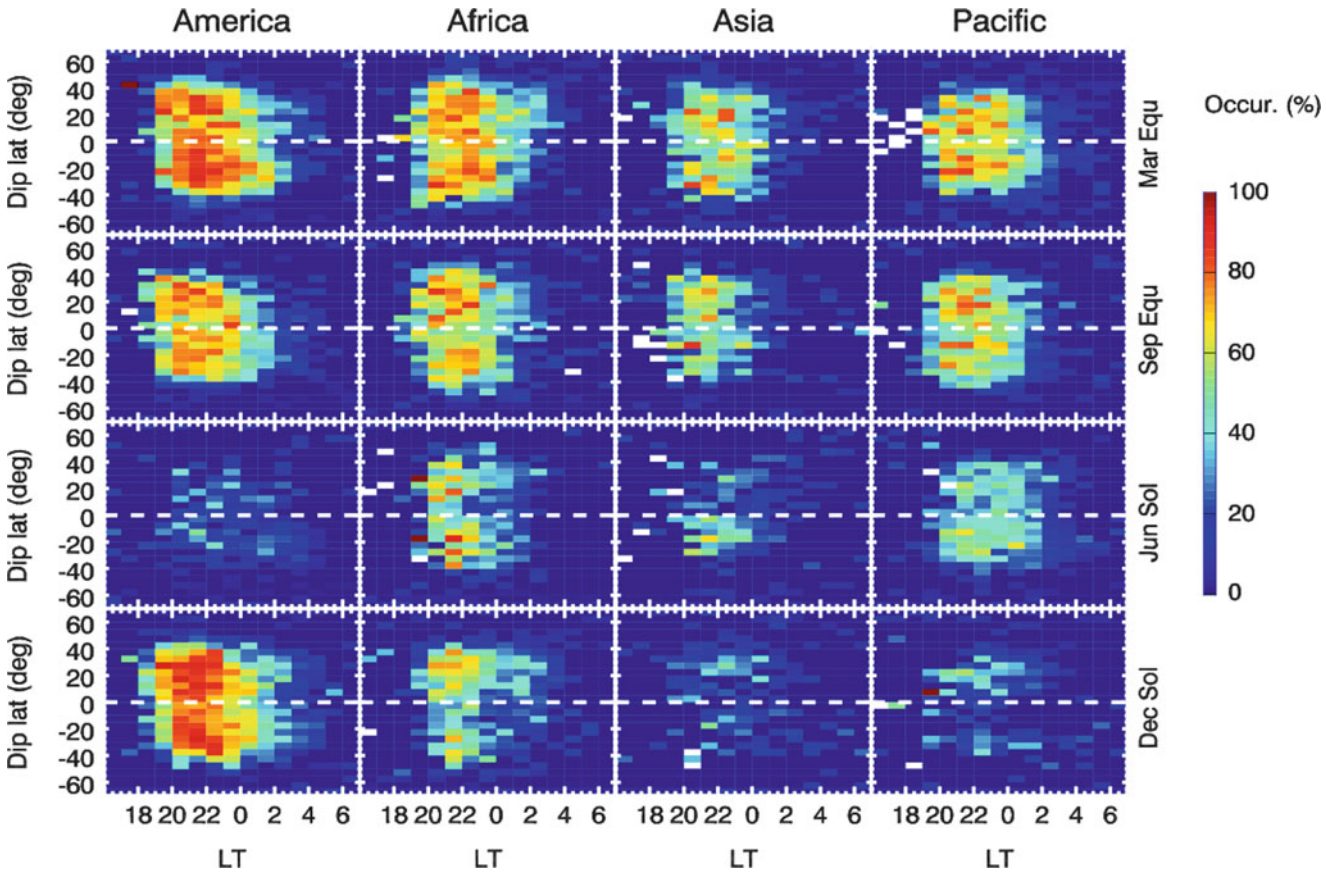

Fig. 4 The dip latitude—local time extent of the equatorial F-region (altitude 170–400 km) irregularities during low-geomagnetic activity periods (i.e. Kp ≤ 3) for different longitude sectors (*columns*) and seasons (*rows*) between 2007 and 2010. Each longitude sector is 90° wide, with −20°E as the eastern edge of the American sector for reference, and each season is represented by the 3-month period surrounding the equinox and solstice months. The cells are coloured according to the percentage occurrence of events with s4max9s ≥ 0.3

promising results and has paved the way for further significant developments towards the objectives of this project. The paper has also highlighted the critical need for, and what can be achieved through, a wide inter/intra-disciplinary international collaboration.

Acknowledgements The authors would like to gratefully acknowledge the Australian government's research grant support for this project through the Australian Space Research Program (ASRP) project.

References

Anthes RA et al (2008) The COSMIC/FORMOSAT-3 mission: early results. BAMS 89:313–333

Bennett JC, Sang J (2011) Modelling the evolution of the low-earth orbit debris population. In: Proceedings of the 11th Australian space science conference, Canberra, 26–29 September 2011

Burke WJ, Gentile LC, Huang CY, Valladares CF, Su SY (2004) Longitudinal variability of equatorial plasma bubbles observed by DMSP and ROCSAT-1. J Geophys Res 109:A12301. doi:10.1029/2004JA010583

Carter BA, Zhang K, Norman R, Kumar VV, Kumar S (2013) On the occurrence of equatorial F-region irregularities during solar minimum using radio occultation measurements. J Geophys Res Space Phys 118:892–904. doi:10.1002/jgra.50089

Hajj GA, Kursinski ER, Romans LJ, Bertiger WI, Leroy SS (2002) A technical description of atmospheric sounding by GPS occultation. J Atmos Sol Terr Phys 64:451–469

Kessler DJ, Cour-Palais BG (1978) Collision frequency of artificial satellites: the creation of a debris belt. J Geophys Res 83(A6):2637–2646

Ko CP, Yeh HC (2010) COSMIC/FORMOSAT-3 observations of equatorial F region irregularities in the SAA longitude sector. J Geophys Res 115, A11309

Kursinski ER, Hajj GA, Schofield JT, Linfield RP, Hardy KR (1997) Observing earth's atmosphere with radio occultation measurements using GPS. J Geophys Res 102(D19):23429–23465

Leroy SS, North JR (2000) The application of COSMIC data to global change research. Terr Atmos Oceanic Sci 11(1):187–210

Le Marshall J, Xiao Y, Norman R, Zhang K, Rea A, Cucurull L, Seecamp R, Steinle P, Puri K, Le T (2010) The beneficial impact of radio occultation observations on Australian region forecasts. Aust Meteorol Oceanogr J 60:121–125

Le Marshall J, Xiao Y, Norman R, Zhang K, Rea A, Cucurull L, Seecamp R, Steinle P, Puri K, Le T (2012) The application of radio occultation for climate monitoring and numerical weather prediction in Australian region. Aust Meteorol Oceanogr J 62:323–334

Norman RJ, Le Marshall J, Carter BA, Wang C-S, Gordon S, Zhang K (2012a) A new pseudo three-dimensional segment method analytical ray tracing (3-D SMART) technique. IEEE Trans Antennas Propag 60(12):5818–5824

Norman RJ, Dyson PL, Yizengaw E, Le Marshall J, Wang C, Carter B, Wen D, Zhang K (2012b) Radio occultation measurements from the Australian micro satellite FedSat. IEEE Trans Geosci Remote Sensing. doi:10.1109/TGRS.2012.2194295

Norman RJ, Bennett JA, Dyson PL, Le Marshall J, Zhang K (2013) A ray-tracing technique for determining ray tubes in anisotropic media. IEEE Trans Antennas Propag 61(5):2664–2675

Pavelyev AG, Zhang K, Wickert J, Schmidt T, Liou YA, Gubenko VN, Pavelyev AA, Salimzjanov RR, Kuleshov Y (2012) Identification and localization of layers in the ionosphere using the eikonal and amplitude of radio occultation signals. Atmos Meas Tech 5:1–16

Sang J, Smith C, Zhang K (2011) Modification of atmospheric mass density model coefficients using space tracking data – a simulation study for accurate debris orbit prediction. Paper AAS 11-205, 21st AAS/AIAA space flight mechanics meeting, New Orleans, 13–17 February 2011

Sang J, Smith C, Zhang K (2012) Towards accurate atmospheric mass density determination using precise positional information of space objects. Adv Space Res 49(6):1088–1096

Tsunoda RT (1985) Control of the seasonal and longitudinal occurrence of equatorial scintillations by the longitudinal gradient in the integrated E-region Pederson conductivity. J Geophys Res 85:722–726

Zhang K, Le Marshall J, Norman R, Wang CS, Fu EJ, Li Y, Kuleshov Y (2010) A study on the relationship between ionospheric correction and data control for GPS radio occultation in Australia. IEEE international symposium on geoscience and remote sensing IGARSS, pp 2940–2943

Zhang K, Fu E, Silcock D, Wang Y, Kuleshov Y (2011) An investigation of atmospheric temperature profiles in the Australian region using collocated GPS radio occultation and radiosonde data. Atmos Meas Tech 4:2087–2092

Simulating GPS Radio Occultation Using 3-D Ray Tracing

R. Norman, J. Le Marshall, K. Zhang, C.S. Wang, B.A. Carter, Y. Li, and S. Gordon

Abstract

Numerical 3-D ray tracing techniques are commonly used for calculating the path of an electromagnetic signal in a medium specified by a refractive index that depends upon position. Numerical ray tracing is an important tool for applications of L-band frequency propagation such as GPS Radio Occultation (RO), where accurate and near real-time results are required. In this study, 3-D numerical ray tracing techniques are used to simulate GPS signals received by the Low Earth Orbit (LEO) satellites and to investigate their variability as a function of time and position due to the refractivity gradients in the ionosphere and the lower atmosphere. The GPS signal paths from the GPS to LEO satellites are simulated with an emphasis on the signal paths propagating through regions of the ionosphere where the refractive gradients are greatest. The effects of the Earth's magnetic field on the L-band RO propagation paths are also investigated.

Keywords

Ionosphere • Refractivity • Ray tracing • Radio occultation

1 Introduction

GPS Radio Occultation (RO) is an emerging space-based Earth observation technique with the potential for atmospheric profiling and meteorological applications. GPS RO uses GPS receivers onboard Low Earth Orbit (LEO) satellites to measure the radio signals transmitted from GPS satellites. The GPS consists of about 30 satellites traveling at an altitude of ~20,200 km orbiting the Earth twice a day and continually transmit signals at the L-band frequencies 1.57542 GHz (L1), 1.2276 GHz (L2) and 1.17645 MHz (L5). Refractive gradients in the ionosphere and atmosphere affect the paths of the L-band electromagnetic signals transmitted from GPS satellites, causing the signals to bend in accordance to Snell's law. The bending of the ray paths in the ionosphere is due to electron density gradients. Refractivity in the lower atmosphere depends mainly upon the atmospheric pressure, temperature and the partial pressure of the water vapour.

The RO technique was initially developed for sounding planetary atmospheres and has aided NASA's planetary exploration programs to Venus, Mars and the outer planets (Fjeldbo et al. 1971; Phinney and Anderson 1968; Bird et al. 1992). The technique has been applied to determine the structure of the Earth's lower atmosphere and ionosphere (Hajj et al. 1994; Healy and Eyre 2000; Hardy et al. 1993; Hernandez-Pajares et al. 2000; Rocken et al. 1997) and to advance meteorological research (Cucurull et al. 2007; Le Marshall et al. 2010, 2012; Zhang et al. 2011).

R. Norman (✉) • K. Zhang • C.S. Wang • B.A. Carter • Y. Li • S. Gordon
Satellite Positioning for Atmosphere, Climate and Environment (SPACE) Research Centre, RMIT University, Melbourne, VIC, Australia
e-mail: robert.norman7@gmail.com

J. Le Marshall
Satellite Positioning for Atmosphere, Climate and Environment (SPACE) Research Centre, RMIT University, Melbourne, VIC, Australia

Bureau of Meteorology, Melbourne, VIC, Australia

C. Rizos and P. Willis (eds.), *Earth on the Edge: Science for a Sustainable Planet*, International Association of Geodesy Symposia 139, DOI 10.1007/978-3-642-37222-3_4,

Ionospheric RO retrievals and corrections remain a major challenge for the overall GPS RO technique. Atmosphere and ionosphere retrieval methods assume local spherical symmetry of the refractivity. The RO retrieval techniques fail to take into consideration the significant spatial and temporal variations in the ionospheric horizontal and vertical electron density gradients and the refractivity gradients in the lower atmosphere. At present, retrieval techniques do not take into account the birefringence effects on the signals in the ionosphere caused by the Earth's magnetic field.

The ionosphere is the region of the Earth's upper atmosphere located at altitudes between 60 and 1,500 km and is normally considered as the transition zone between our atmosphere and outer space, its primary source of ionization is incident ultra violet solar radiation. The ionosphere is highly dynamic and the study of "space weather" or "space climate" refers to the ionosphere's important connection to the Earth's atmosphere and its dynamic nature. The ionosphere thickens, changes its density, and supports a wide range of traveling disturbances, generated by the flux of incident ionizing solar radiation. The dynamic nature of the ionosphere is apparent on timescales of minutes and hours, as well as diurnally and seasonally. Some of the major features of the ionosphere are the ionospheric electron density layers, equatorial anomaly, troughs of ionization and a range of traveling ionospheric disturbances.

This study focuses on GPS signal propagation and in particular the ionospheric and atmospheric effects on GPS signals. A new 3-D numerical ray tracing technique (Norman et al. 2013), based on Haselgroves equations, utilizing geometrical optics principles in anisotropic media is used to trace the GPS ray paths. Ray tracing techniques are commonly used for calculating the path of an electromagnetic signal in a medium specified by a position-dependent refractive index. In this study numerical 3-D ray tracing is used to trace L-band frequency paths with a sophisticated ionospheric model, namely the International Reference Ionosphere (IRI-2007) (Bilitza and Reinisch 2008). The effects due to ionospheric gradients and the Earth's magnetic field on GPS signal paths that are initialized with a negative elevation angle will be investigated. A simple exponential function with a scale height of 7.5 km and ground refractivity of 300 N-units is used to represent the lower atmosphere.

The phase refractive index in the ionosphere (n) is given by the Appleton–Lassen equation:

$$n^2 = 1 - \frac{X}{1 - iZ - \frac{Y_T^2}{2(1-X-iZ)} \pm \frac{1}{1-X-iZ}\sqrt{\left(\frac{Y_T^4}{4} + Y_L^2(1-X-iZ)^2\right)}} \tag{1}$$

where

X is proportional to the electron density,

Y is proportional to the Earth's magnetic field (longitudinal Y_L and transverse Y_T components)

Z is proportional to the collision frequency (ignored)

"+" generally represents the ordinary (O) mode and "−" generally represents the extraordinary (X) mode.

Refractivity $N = (n-1) \times 10^6$ (N-units)

2 Results

The 3-D numerical ray tracing program incorporates the IRI-2007 model for the electron density in the ionosphere and a special version of the POGO 68/10 magnetic field Legendre model (found in the IRI-2007). Ray tracing was performed between a GPS and LEO satellite. The GPS satellite used had fixed geomagnetic coordinates (−66.4ºN, 164ºE) and was positioned to observe geomagnetic northward propagation. The LEO satellite utilized had an orbital altitude of 800 km. Ray tracing was performed for day 207 in year 2010 as inputs to the IRI-2007. Figure 1 shows the electron density with respect to height and geomagnetic latitude, for the fixed geomagnetic longitude 164ºE and ∼1200 LT (local time). Notice the latitudinal, altitudinal and diurnal variations in the refractivity. The chosen ray tracing model constraints highlight the equatorial anomaly and the gradients in electron density. At night, ionosphere electron densities are weak; therefore the magnitude of the refractivity is reduced. This is evident in Fig. 2, which shows a vertical profile of the refractivity at 1200 LT and geomagnetic coordinates 35ºN, 164ºE. These coordinates represent the tangent point where the perigee height is ∼100 km. The data points are in steps of 3 km starting from a height of 3 km up to a height of 870 km. The refractivity in the lower atmosphere is significant at heights < 30 km. The ionosphere is a dispersive medium and Fig. 2 shows the profiles of refractivity for the L1 and L2 band GPS frequencies. Figure 2 shows the GPS L1 band frequency, refractivity profiles of the ionosphere and how it can change both spatially and temporally. The green profile in Fig. 2 corresponds to the refractivity at geomagnetic coordinates 164ºE, 0ºN at 1200 LT.

From Fig. 2 the refractivity in the ionosphere is negative, refer to (1). At heights from 40 to 80 km refractivity is close to zero. The refractivity at the Earth's surface is approximately 300 N-units and decreases exponentially in the

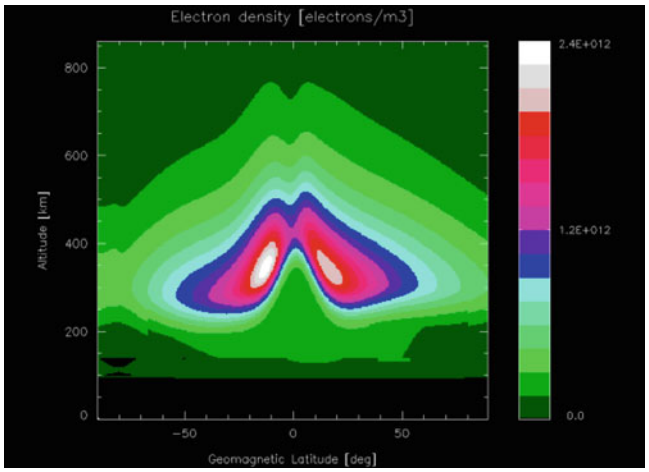

Fig. 1 Electron density from IRI-2007 for a geomagnetic longitude 164ºE, 1200 LT, day 207 and year 2010

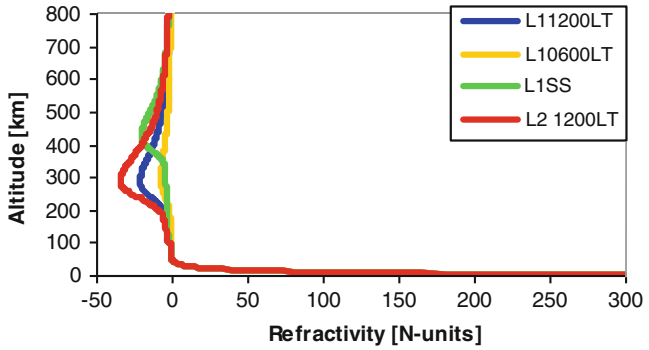

Fig. 2 Refractivity for a geomagnetic coordinates 164ºE, 35ºN at 0600 and 1200 LT and 164ºE, 0ºN at 1200LT for L1SS

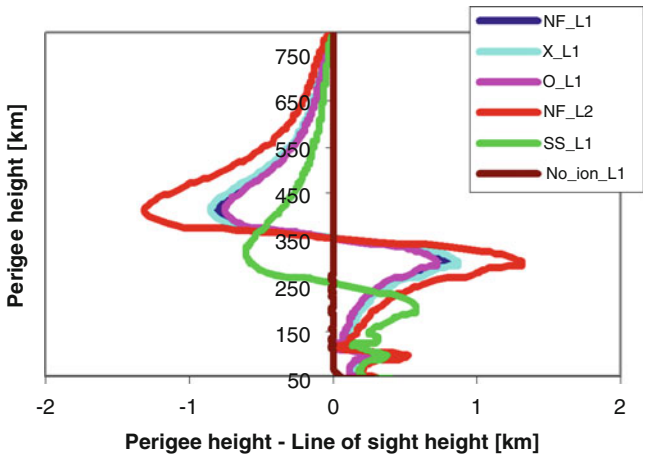

Fig. 3 RO ray tracing results showing perigee height versus perigee height—line of sight height

troposphere and stratosphere with a scale height of 7.5 km. The refractivity follows (1) above an altitude of 60 km.

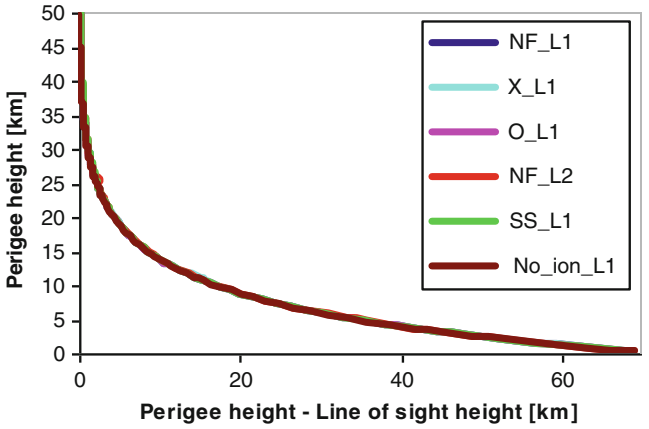

Fig. 4 RO ray tracing results showing perigee height versus perigee height—line of sight height, below a perigee height of 50 km

The impact parameter and tangent point are important parameters in RO retrieval algorithms. The impact parameter is the height of the closest approach of a ray path to the Earth's surface and the tangent point is the ground position of the impact parameter. In ray tracing this point of closest approach of a ray path to the Earth's surface is called the perigee height. In classical RO as the ray path traverses the ionosphere and atmosphere the impact parameter is shown to be above the line of sight between the GPS and LEO satellites. Ray tracing has proven this assumption incorrect (Norman et al. 2012), as the results in Fig. 3 clearly show that RO ray paths can be below the line of sight i.e., perigee height—line of sight < 0. Ray paths not traversing below hmF2 (height maximum of the F2 layer) will bend upwards as the lower parts of the signal path will be in a region of slightly higher electron density, thus lower refractivity, and will travel faster causing the signal to refract upwards away from the Earth. Figure 3 shows perigee heights versus the difference in perigee height when no refractive gradients are present. Ray tracing results are shown for the GPS L1 and L2 band frequencies as well as the L1 no field (NF), ordinary (O), extraordinary (X) and spherically stratified (SS) ionosphere paths. Notice that the O and X perigee heights are either side of the NF perigee heights. Figure 4 shows the results below 50 km, where the difference in perigee height and the line of sight height can be as much as 70 km due to the increased refractivity in the troposphere and boundary layer.

From Fig. 3 the differences in perigee height from the line of sight height in the ionosphere is less than 2 km. Figure 5 shows a zoomed in section of Fig. 4. From Fig. 5 the difference in perigee height can be tens of meters away from the true value if the ionosphere ignored.

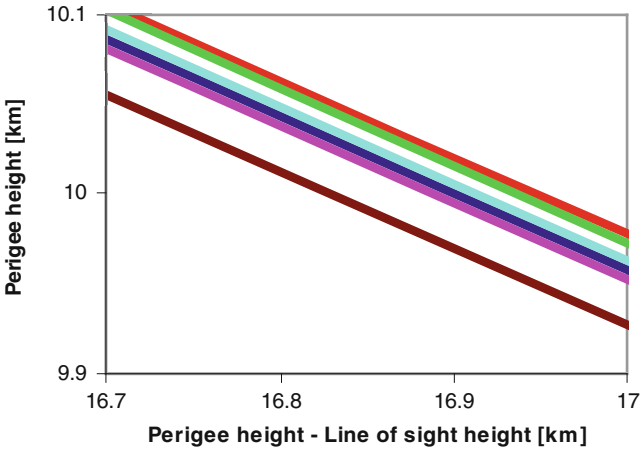

Fig. 5 A zoomed in section from Fig. 4

3 Conclusion

The effects of ionospheric gradients and birefringence on GPS L-band frequency RO propagation paths were investigated. In this study geomagnetic northward propagating signals were studied using a 3-D ray tracing technique incorporating the IRI-2007 and the POGO 68/10 magnetic field model to simulate RO ray paths. It was found that refractive gradients in the ionosphere can cause the perigee heights in the ionosphere to be below the GPS to LEO line of sight height. For RO ray paths with a perigee height of 10 km the ionosphere contributes ∼50 m change to the perigee height and the magnetic field contributes ∼15 m. Ray tracing combined with the best available ionospheric and magnetic field models is important for understanding the contributions of ionospheric gradients, atmospheric gradients and the Earth's magnetic field on GPS RO propagation paths.

Acknowledgements This work is supported in part by the Australian Space Research Program project of "Platform Technologies for Space, Atmosphere and Climate" endorsed to a research consortium led by RMIT University.

References

Bird MK, Asmar SW, Brenle JP, Edenhofer P, Funke O, Patzoid M, Volland H (1992) Ulysses radio occultation observations of the Io plasma torus during the Jupiter encounter. Science 257:1531–1535

Bilitza D, Reinisch B (2008) International reference ionosphere 2007: improvements and new parameters. Adv Space Res 42(4):599–609

Cucurull L, Derber JC, Treadon R, Purser RJ (2007) Assimilation of global positioning system radio occultation observations into NCEP's global data assimilation system. Mon Weather Rev 135:3174–93

Fjeldbo G, Kliore AJ, Eshleman VR (1971) The neutral atmosphere of Venus as studied with Mariner V radio occultation experiments. Astron J 76:123–140

Hajj GA, Ibanez-Meier R, Kursinski ER, Romans LJ (1994) Imaging the ionosphere with global positioning system. Int J Imaging Syst Technol 5:174–184

Hardy KR, Hajj GA, Kurinski ER (1993) Accuracies of atmospheric profiles obtained from GPS occultations. In: Proceedings of the ION-GPS 93 conference, Institute of Navigation, Salt Lake City, pp 1545–1557

Healy SB, Eyre JR (2000) Retrieving temperature, water vapor and surface pressure information from refractive index profiles derived by radio occultation: a simulation study. Q J R Meteorol Soc 126:1661–83

Hernandez-Pajares M, Juan JM, Sanz J (2000) Improving the Abel inversion by adding ground GPS data to LEO radio occultations in ionospheric sounding. Geophys Res Lett 27:2473–2476

Le Marshall J, Xiao Y, Norman R, Zhang K, Rea A, Cucurull L, Seecamp R, Steinle P, Puri K, Le T (2010) The beneficial impact of radio occultation observations on Australian region forecasts. Aust Meteorol Oceanogr J 60:121–125

Le Marshall J, Xiao Y, Norman R, Zhang K, Rea A, Cucurull L, Seecamp R, Steinle P, Puri K, Le T (2012) The application of radio occultation for climate monitoring and numerical weather prediction in Australian region. Aust Meteorol Oceanogr J 62:323–334

Norman RJ, Bennett JA, Dyson PL, Le Marshall J, Zhang K (2013) A ray-tracing technique for determining ray tubes in anisotropic media. IEEE Trans Antennas Propag 61(5):2664–2675

Norman RJ, Dyson PL, Yizengaw E, Le Marshall J, Wang C-S, Carter B, Wen D, Zhang K (2012) Radio occultation measurements from the Australian micro satellite FedSat. IEEE Trans Geosci Remote Sensing 50(11):4832–4839. doi:10.1109/TGRS.2012.2194295

Phinney RA, Anderson DL (1968) On the radio occultation method for studying planetary atmospheres. J Geophys Res 73:1819–1827

Rocken C, Anthes R, Exner M, Hunt D, Sokolovskiy S, Ware R, Gorbunov M, Schreiner W, Feng D, Herman B, Kuo Y, Zou X (1997) Analysis and validation of GPS/MET data in the neutral atmosphere. J Geophys Res 102:29849–29866

Zhang K, Fu E, Silcock D, Wang Y, Kuleshov Y (2011) An investigation of atmospheric temperature profiles in the Australian region using collocated GPS radio occultation and radiosonde data. Atmos Meas Tech 4:2087–2092

Near Real Time Estimation of Integrated Water Vapour from GNSS Observations in Hungary

Sz. Rózsa, A. Kenyeres, T. Weidinger, and A.Z. Gyöngyösi

Abstract

Meteorological products derived from Global Navigation Satellite Systems (GNSS) observations have been routinely used for numerical weather prediction in several regions of the world. Hungary would like to join these activities exploiting meteorological usage of the dense GNSS CORS (Continuously Operating Reference Station) network operated by the Institute of Geodesy, Cartography and Remote Sensing for positioning applications.

This paper introduces the near real-time processing system of GNSS observations for meteorological purposes in Hungary. The hourly observations of 35 Hungarian permanent GNSS CORSs are processed. This network is extended beyond the country with about 50 stations covering Eastern and Central Europe. The data analysis is being done using the Bernese V5.0 GPS data processing software. The Hungarian CORS network has an average baseline length of 60 km, thus the precipitable water vapour (PW) can be estimated with a high spatial resolution.

The estimation of the PW from the zenith wet delay (ZWD) is carried out in near real-time. Firstly, the zenith hydrostatic delays (ZHD) are subtracted from the total delays. The wet delays are then scaled to precipitable water vapour values.

The GNSS derived PW values were validated using radiosonde observations over Central Europe using the observations of a 47-day-long period (April 14–May 31, 2011). The results showed that the estimated PW values agree with radiosonde observations at the level of ± 1.5 mm in terms of standard deviation. In this comparison a bias of $+1.0$ mm was observed. Following the validation phase, our analysis will be connected to the continental E-GVAP project (GNSS Water Vapour Programme of the Network of European Meteorological Services, EUMETNET).

Keywords

CORS • GNSS meteorology • Integrated water vapour • Numerical weather prediction • Radiosounding

Sz. Rózsa (✉)
Department of Geodesy and Surveying, Budapest University of Technology and Economics, Muegyetem rkp. 3, H-1111 Budapest, Hungary
e-mail: szrozsa@agt.bme.hu

A. Kenyeres
Satellite Geodetic Observatory, Institute of Geodesy, Cartography and Remote Sensing, P.O. Box 585, H-1592 Budapest, Hungary

T. Weidinger • A.Z. Gyöngyösi
Department of Meteorology, Eötvös Lóránd University, P.O. Box 3, H-1518 Budapest, Hungary

C. Rizos and P. Willis (eds.), *Earth on the Edge: Science for a Sustainable Planet*, International Association of Geodesy Symposia 139, DOI 10.1007/978-3-642-37222-3_5,

1 Introduction

The water vapour content of the atmosphere plays an important role in many meteorological applications. On a short term it is applied for numerical weather predictions to predict the intensity of rainfalls. However, on a long term the water vapour plays a significant role in climatic analyses, since it is the most important greenhouse gas.

The atmospheric water vapour content can be measured with different techniques, like radiosoundings, microwave radiometers and GNSS, etc. Currently the most reliable technique is the radiosounding. In this case the vertical temperature, pressure and humidity profiles are measured, and the water vapour content of the atmospheric column is computed by vertically integrating the water vapour density. However, radiosondes have significant disadvantages: they are quite costly and they are also prone to systematic biases and calibration problems. Due to the high costs, radiosonde profiles are measured with the period of 24 h at only two stations in Hungary (Budapest and Szeged).

Since the active GNSS network has been established in Hungary, the feasibility of the estimation of the PW from GNSS observations is studied in this paper. Similar studies have been reported by researchers from the Central European countries (e.g. Karabatic et al. 2011; Bosy et al. 2010; Igondova and Cibulka 2010). Our study focuses on the development of a near real-time processing and validation system, which automatically processes the hourly observations of the GNSS stations. Moreover, it also validates the estimates with the PW values and other parameters computed from the radiosonde profiles.

The purpose of this work is to take the first step towards the integration of PW values estimated from GNSS observations in the numerical weather prediction (NWP) models used in Hungary. The near real-time estimation of PW from GNSS data would significantly improve the spatial and temporal resolution of the observed PW values. Thus the highly variable atmospheric water vapour could be modelled with a higher accuracy without additional costs. This could improve the accuracy of predicting heavy rainfall in Hungary. The establishment of a near real-time processing facility would also enable us to join the EUMETNET E-GVAP Programme (Vedel 2006).

The first part of this paper introduces the structure of the processing software. The methodology of the PW estimations is then discussed, followed by the methodology of the validation. The validation is carried out using all of the quantities used in the estimation of the PW. The results of these validations are also presented in the last part of the paper.

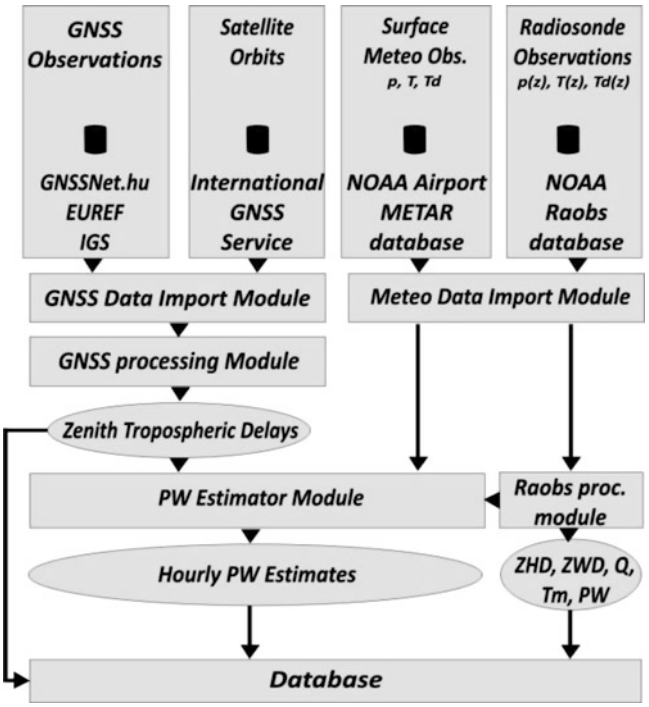

Fig. 1 The block scheme of the near real-time data processing and validation system

2 The Near Real-Time Processing and Validation System

The processing system is responsible for collecting and processing the GNSS observations in near real-time. Apart from that, surface meteorological observations are collected and processed routinely for the estimation of PW, and the observed radiosonde profiles are used to compute the PW for validation purposes. The most important features of the system are briefly introduced in this section.

In order to evaluate the potential of the PW derived from the active GNSS CORS network, a near real-time processing and validation system has been developed. The core functionality is provided by the Bernese GNSS data processing software version 5.0 (Dach et al. 2007). The block scheme of the system can be seen in Fig. 1.

Firstly, the *GNSS Import Module* collects the GNSS observations from various data centres:

- The GNSS CORS network of Hungary consisting 50 stations (GNSSNet.hu);
- The GNSS Data Centre maintained by the German Federal Agency for Cartography and Geodesy (BKG), where altogether 20 EPN (EUREF Permanent Network) stations and 23 IGS (International GNSS Service) stations where chosen for the data processing.

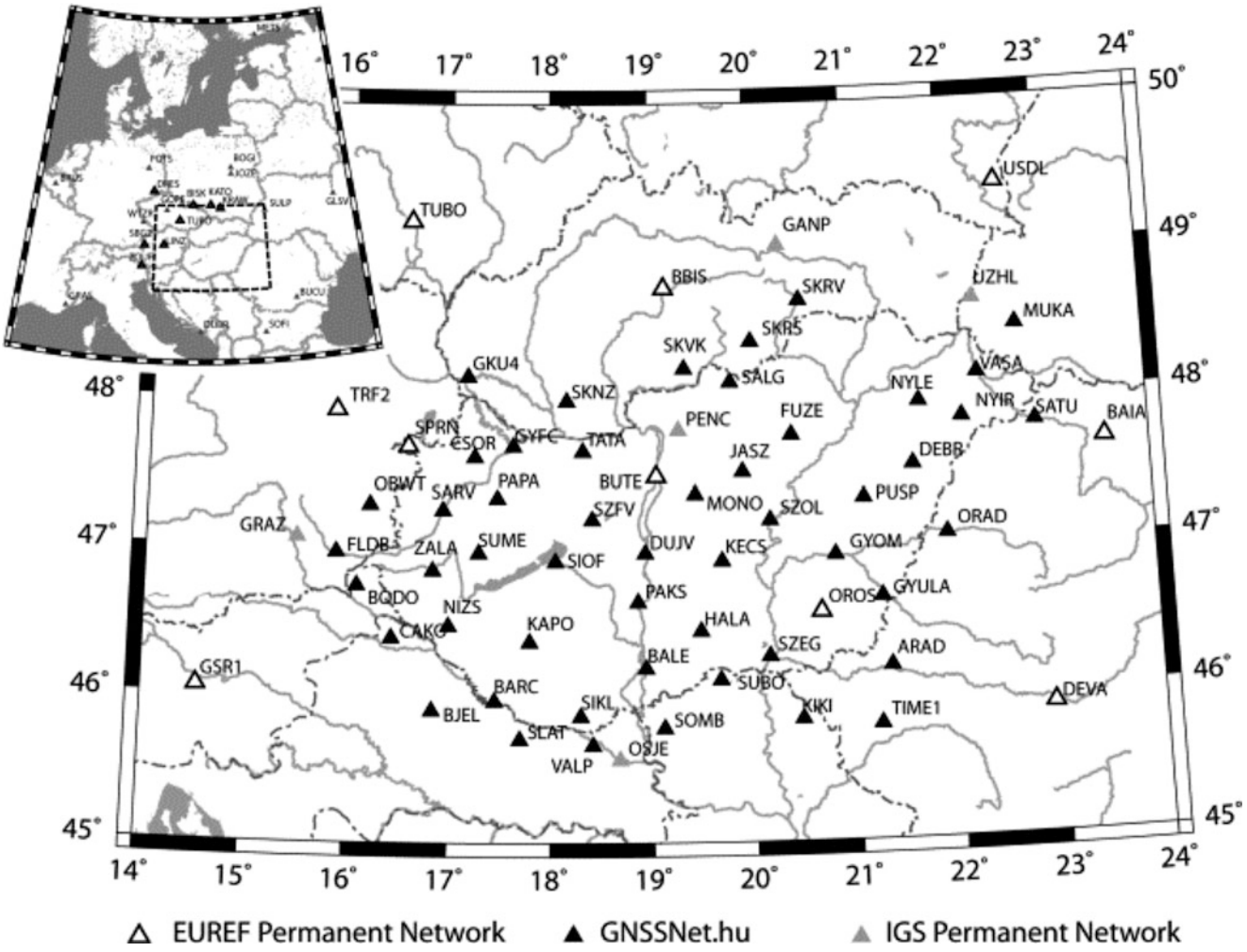

Fig. 2 The GNSS CORS network processed

The processed CORS network consists of 93 stations. The network can be seen in Fig. 2.

Secondly the ultra-rapid products (orbits, clocks and Earth orientation parameters) are collected from the IGS. Afterwards the GNSS data are processed by the *GNSS Processing Module*. In each hour, the observations of the previous 12 h are concatenated and processed using fixed station coordinates. Although both GPS and GLONASS observations are collected in the network, currently only the GPS observations are processed routinely. Zenith tropospheric delays (ZTD) are estimated on an hourly basis using the Saastamoinen model (Saastamoinen 1972, 1973) for modelling the "a priori" zenith hydrostatic delay (ZHD) and the Niell mapping function to map the zenith delays to the satellite direction. Horizontal tropospheric gradients are estimated along with the ZWDs using a 0° elevation mask. Currently the GNSS data processing starts 15 min after the full hour and lasts for approximately 50 min.

The *Meteo Data Import Module* is responsible for collecting surface meteorological observations including total air pressure (p), surface temperature (T) and dewpoint (T_d) from the Airport METAR (**ME**teorological **T**erminal **A**viation **R**outine Weather Report) Database maintained by the National Oceanic and Atmospheric Administration (NOAA). The hourly METAR observations are decoded and stored in a database for further use. Furthermore, the radiosonde profiles are collected on a daily basis from the NOAA Raobs (Radiosonde Observations) database. Altogether the profiles from 23 radiosonde launching sites are used for validation purposes (Fig. 3).

The *PW Estimator Module* computes the PW based on the estimated ZTD from the GNSS data processing and the surface total air pressure. In order to validate the estimated PW, the collected radiosonde profiles are processed by the *Raobs Processing Module*. All of the results are stored in a relational database for further analysis.

Fig. 3 The processed radiosonde launching sites

3 Methodology

This section focuses on the methodology of the estimation of PW. Moreover various aspects of the validation process are also discussed here.

3.1 The Estimation of PW

The *ZTD*s are used as an input for the *PW Estimator Module*. In order to convert the estimated *ZTD* to *PW*, firstly the *ZHD* must be subtracted:

$$ZWD = ZTD - ZHD, \tag{1}$$

where *ZWD* is the zenith wet delay. The *ZHD* is computed from the total air pressure (p) at the mean sea level using the Saastamoinen-model (Saastamoinen 1972, 1973):

$$ZHD = 0.002277\,p \tag{2}$$

Since the total air pressure is not observed at the majority of GNSS stations, it should be either estimated using NWP models or it should be interpolated from the observations of the automatic meteorological stations of the meteorological services.

Currently our system utilizes the first option, namely the DBCRAS (Direct Broadcast CIMSS Regional Assimilation System) NWP model (Aune et al. 2008) from the Department of Meteorology of the Eötvös Lóránd University, that provides hourly forecasts of the total air pressure at the mean sea level, the surface total air pressure as well as the surface temperature. This NWP model has a resolution of 48 km × 48 km, which is suitable for the computation of ZHDs. In the near future the integration of a second NWP model is planned, since the Department of Meteorology runs the WRF (Weather Research and Forecasting) model with a higher resolution but with a smaller coverage (covering an area of 100 km beyond the borders of Hungary).

Based on the computed value of the ZWD, the PW can be estimated using an appropriate scaling factor (Q) (Haase et al. 2003):

$$PW = \frac{ZWD}{Q}. \tag{3}$$

The scaling factor Q is dimensionless, since both the PW and the ZWD are expressed in mm. In our computation Q is computed as a direct function of the surface

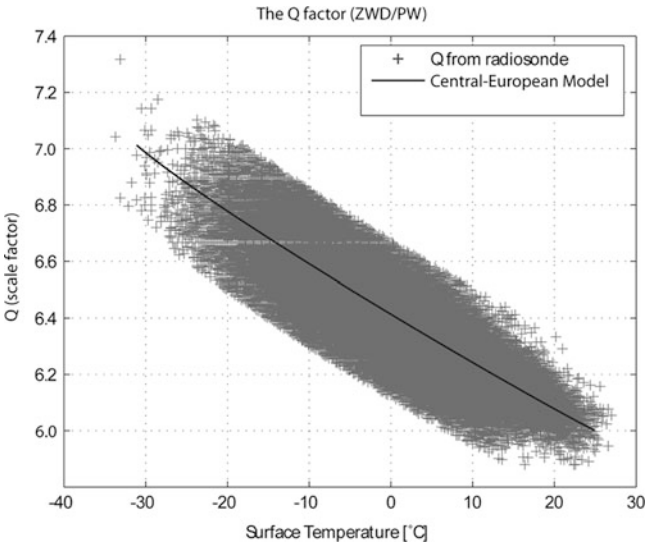

Fig. 4 The second order polynomial of surface temperature fitted to the scale factor values computed from radiosonde observations

temperature based on a regression analysis of more than 150,000 radiosonde observations in the area (Fig. 4):

$$Q = a_0 + a_1\left(T - \bar{T}\right) + a_2\left(T - \bar{T}\right)^2 \tag{4}$$

where T is the surface temperature in Kelvin, while a_0, a_1, a_2 and $\bar{T}$ are empirical constants with the following values (Rózsa et al. 2012):

$$\begin{aligned} a_0 &= 6.3953 \pm 0.0003, \\ a_1 &= -1.75 \times 10^{-2} \pm 2.7 \times 10^{-5}\ \ [1/\mathrm{K}], \\ a_2 &= 7.5 \times 10^{-5} \pm 2.5 \times 10^{-6}\ \left[1/\mathrm{K}^2\right], \\ \bar{T} &= 283.17\quad [\mathrm{K}]\ . \end{aligned} \tag{5}$$

A similar model has been proposed by Emardson and Derks (2000) based on more than 100,000 radiosonde observations in Europe. However other investigations showed that the locally fitted model performs better than the Emardson–Derks model in the area of Hungary (Rózsa et al. 2012).

It must be noted that Bevis et al. (1992) proposed a different method for the computation of the scale factor Q:

$$Q(T_m) = \frac{10^6}{R_v\left(-\frac{R_d}{R_v}k_1 + k_2 + \frac{k_3}{T_m}\right)}, \tag{6}$$

where R_v and R_d are the specific gas constants of water vapour and dry air respectively and T_m is the mean temperature of water vapour. Bevis et al. (1992) proposed the following formula for the computation of T_m as a function of the observed surface temperature:

$$T_m = 70.2 + 0.72T, \tag{7}$$

Since this approach is widely used in practice, both the Q and T_m parameters are computed from radiosonde profiles for validation purposes.

3.2 Validation with Radiosonde Observations

Our aim was to provide the near real-time PW estimates from the GNSS observations. Besides the automatic validation of these results was carried out. In order to achieve this, the available radiosonde observations are routinely acquired from the NOAA Raobs database. In order to be able to validate the computational procedure and the results of PW estimations, a number of parameters are computed from the radiosonde observations. The most important ones are the *PW*, *ZWD*, *ZHD* values and the scale factor Q. Since this scale factor is computed as a function of the surface temperature, the approaches introduced in the previous section can be evaluated, too.

Computation of PW from Radiosonde Profiles

Radiosonde observations provide the vertical temperature, dew point and pressure profiles (along with the wind speed and wind directions). The PW in a layer between two radiosonde observations $i-1$ and i can be computed using the mixing ratio and the total air pressure:

$$PW_i = \frac{1}{g}\left(p_{i-1} - p_i\right)\frac{MR_{i-1} + MR_i}{20}, \tag{8}$$

where g is the gravity gradient at the mean altitude of the layer, and *MR* is the mixing ratio, which can be computed from the observed total air pressure and the partial pressure of water vapour (e) (WMO 2008):

$$MR = 622 \times \frac{e}{p - e}, \tag{9}$$

The total *PW* in a vertical column can be computed by summing up the *PW* in the layers of the atmospheric column.

Computation of ZHD and ZWD from Radiosonde Profiles

The tropospheric delay (TD) can be computed by integrating the refractivity (N) along the path of the incoming satellite signal (Thayer 1974). Introducing the Essen and

Froome (1951) formula for the refractivity, the following equation is obtained:

$$TD = 10^{-6} \int N \, \mathrm{ds} = 10^{-6} \int \left(k_1 \frac{p_d}{T} + k_2 \frac{e}{T} + k_3 \frac{e}{T^2} \right) \mathrm{dz}, \quad (10)$$

where p_d is the partial pressure of dry air, k_1, k_2 *and* k_3 are empirical constants with the values of 0.7760 K/Pa, 0.704 K/Pa and 0.03739×10^5 K^2/Pa respectively. The refractivity can be split into the dry and the wet parts (Smith and Weintraub 1953). Since the partial pressure of the dry air is not observable, the *TD* in the zenith direction (*ZTD*) can be written as:

$$ZTD = ZHD + ZWD = 10^{-6} \int \left[k_1 \frac{p}{T} \right] \mathrm{dz} + 10^{-6} \int \left[(k_2 - k_1) \frac{e}{T} + k_3 \frac{e}{T^2} \right] dz \, . \quad (11)$$

Although the PW stemming from radiosonde profiles is comparable with the GNSS based estimations, it is not true for the ZHD. Radiosonde profiles terminate at the pressure level of approximately 100 hPa (approximately the altitude of 35 km). However, the neutral upper atmosphere has a non-negligible effect on the ZHD. This must be taken into account, when the ZHDs computed from radiosonde observations and the values estimated by (2) are compared. The correction can be computed from standard atmosphere models as well as from radio occultation observations (Kursinski and Hajj 2001).

The processing system uses the former option based on the International Standard Atmosphere (ISO 2533:1975). Figure 5 shows the ZHD at different elevations. It can be seen that the hydrostatic delay still reaches the level of 1.3 cm even at the elevation of 35 km, where the radiosonde observations usually terminate. This error would cause approximately 2 mm error in the PW estimates. The *Raobs Processing Module* computes the correction of ZHD, thus this effect is taken into account in the estimations.

Computation of the Scale Factor *Q* from Radiosonde Profiles

Since both the PW and the ZWD can be computed from the radiosonde profiles, the reference values of the scale factor Q can be computed using (3). Due to the fact that Q is usually computed either from a polynomial model (4) or a model proposed by Bevis et al. (1992) in (6), the T_m temperature is also computed directly from the radiosonde observations using the following equation:

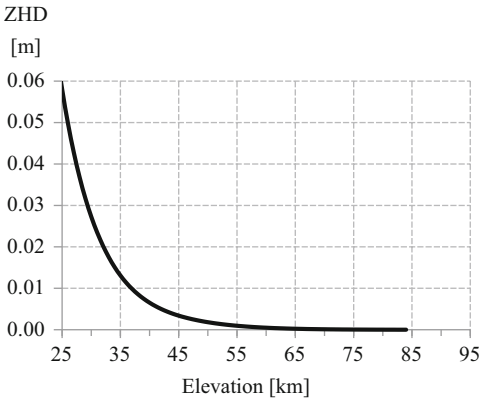

Fig. 5 Zenith hydrostatic delays computed from the International Standard Atmosphere (m)

$$T_m = \frac{\int \rho_v \, \mathrm{dz}}{\int \frac{\rho_v}{T} \, dz}, \quad (12)$$

where ρ_v is the water vapour density:

$$\rho_v = \frac{e}{R_v T}. \quad (13)$$

The computation of the T_m values from radiosonde observations enables us to study various models used for the estimation of the scale factor Q.

The reference values of the aforementioned parameters are automatically computed from the radiosonde profiles, and they are stored in a database along with the lowest observed total pressure and the burst altitude of the sonde. The latter variables are used to assess the reliability of the *ZHD* values derived from the radiosonde observations.

4 Results and Validation

The near real-time data processing system has been established in the premises of the Satellite Geodetic Observatory in Penc. The system started to operate on April 14, 2011. In the following sections the first results of the validation process are presented. This validation has been done using the radiosonde observations taken at Budapest in the period of April 14–May 31.

After processing the GNSS observations, the PW was computed using the predicted surface meteorological parameters obtained from the DBCRAS NWP model. The radiosonde observations were processed according to Sect. 3.2. The results of are shown in the next sections.

Table 1 The statistical properties of the residuals of the zenith hydrostatic delays computed from the Saastamoinen model with respect to radiosonde observations (mm)

	Min	Max	Mean	Std. dev.
Radiosonde-Saastamoinen	−4.1	2.3	−1.4	±1.2

Table 2 The statistical properties of the residuals of the zenith wet delays estimated from the GNSS observations with respect to radiosonde observations (mm)

	Min	Max	Mean	Std. dev.
Radiosonde-GNSS	−30.9	29.2	+1.7	±10.6

Table 3 The statistical properties of the Q factor computed from the surface temperature with respect to the radiosonde observations (the values in brackets are relative values)

	Min	Max	Mean	Std. dev.
Radiosonde-GNSS	−0.36 (−5.5 %)	−0.03 (−0.5 %)	−0.20 (−3.1 %)	±0.08 (±1.2 %)

4.1 Estimation of the Hydrostatic and Wet Delays

Due to the fact that the processing facility computes various tropospheric parameters from the radiosonde observations, the performance of the "a priori" ZHD estimation can also be evaluated. The Saastamoinen model provided a nice fit to the radiosonde observations. The statistical properties of the residuals can be found in Table 1. The table shows that the ZHD is slightly overestimated by the model (−1.4 mm of bias) in the study period. However this bias would cause a systematic error of only −0.2 mm in the PW estimates, since the scale factor Q has the approximate value of 6.5 [see (5)]. This value is well below the expected 1–1.5 mm error of the PW estimations.

On the other hand the GNSS estimated zenith wet delays show a worse fit compared to the radiosonde observations (Table 2.). Although the bias is still in the order of a few millimetres, the standard deviation reaches the level of ±1 cm, which would mean that the accuracy of the PW estimation would be in the order of ±1.5 mm.

4.2 Validation of the Estimation of Scale Factor Q

The PW values are computed from the ZWDs using the scale factor Q (3), that is usually estimated from the surface temperatures using (4) or (6). Since both the PW and the ZWD values are also computed from the radiosonde observations, reference values can be computed from the radiosonde profiles using (3). Thus the scale factor Q estimated from the surface temperatures and computed from the profiles can be compared, too.

The statistics of the comparison can be found in Table 3. The results show that the value of Q is overestimated by 3 % in the study period. This would lead to the underestimation of the PW by 3 %. Since the PW had the mean value of approximately 20 mm during this period, that would mean a bias of −0.6 mm in the estimated value, which is much larger than the effect of the "a priori" model of the hydrostatic delays.

4.3 The Effects of the Coordinate Fixing

Tropospheric delays are estimated based on the fixed coordinates of the GNSS stations. In order to study the effects of the coordinate fixing strategy, different scenarios have been studied. The observations of the period of April 14, 2011 to May 31, 2011 were processed with various strategies. The station coordinates were fixed on:

- The ITRF coordinates computed from ITRF coordinates and station velocities (ITRF);
- The weekly coordinate solutions of the network (ITRF_WK, where the weekly coordinates are computed using all the observations taken from the previous GPS Week);
- A running window combination of the daily observations, where the length of the window varies between 4 and 11 days (RW_LL, where LL is the length of the window in days).

In the last two cases, the normal equations of the least square adjustment of the 12-h-sessions are combined with a minimal constraint approach using IGS stations for datum definition. The major difference between the weekly and the running window strategies is, that the running window strategy with the length of seven days combines the normal equations of the previous 7 days on a daily basis, while the weekly coordinate solutions are generated once a week from all the observations of the previous GPS week.

The PW has been estimated using the aforementioned approaches, and the estimates have been compared to the reference values computed from the radiosonde observations. The standard deviation of the residuals did not show significant differences between the various fixing strategies (the maximal observed difference was only 0.05 mm). However the bias of the PW estimation decreased by 15 %, when the weekly coordinate solutions have been used (Fig. 6). A similar performance was experienced, when a running window of more than 7 days was applied. This window size fits to the average residence time of the water molecules in the atmosphere (Pidwirny 2006).

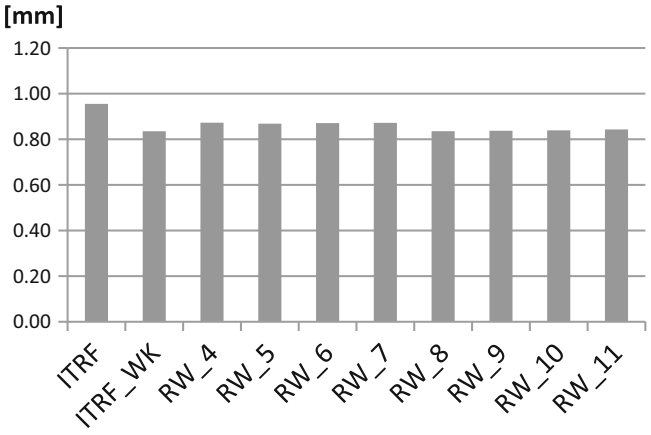

Fig. 6 The bias of the PW estimations using different coordinate fixing strategies

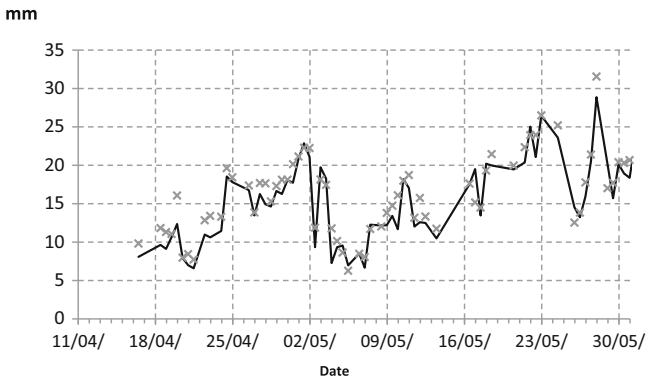

Fig. 7 The precipitable water vapour in the study period (*black line*—GNSS estimates; *grey crosses*—radiosonde observations)

Table 4 The statistical properties of the residuals of the GNSS estimates and ECMWF analysis of PW with respect to the radiosonde observations

	Min	Max	Mean	Std. dev.
Radiosonde-GNSS	−4.2	4.6	1.0	±1.5
Radiosonde-ECMWF	−4.6	4.7	0.4	±1.6

4.4 PW Comparison with Radiosonde Observations and NWP Model

The PW estimates have been compared with radiosonde observations and predictions from ECMWF analysis in the study period. The results can be seen in Fig. 7, while the statistical properties can be found in Table 4.

The results show a remarkable agreement between GNSS estimates and radiosonde observations. The experienced bias of +1.0 mm and standard deviation of ±1.5 mm shows that GNSS tends to underestimate the precipitable water vapour.

The PW estimates have also been compared to the results of ECMWF analysis, too. Table 4. shows that although the ECMWF analysis reproduces the radiosonde based PW estimation with a smaller bias of 0.4 mm, the standard deviations are on the same level in both cases.

5 Conclusions and Outlook

Based on the validation results it can be stated that the PW estimates fit to the radiosonde observations on a similar level compared to other results in the literature (e.g. Karabatic et al. 2011; Bosy et al. 2010; Igondova and Cibulka 2010). It must be noted that the observed standard deviation of the residuals with respect to the radiosonde observations (±1.5 mm), is quite close to the results obtained during the recent radiosonde intercomparison campaigns (±1.0 mm) according to Nash et al. (2011).

Our results provided the best fit, when the fixed coordinates were computed by the weekly combination or the combination of the prior 8–11 days of GNSS observations. This is in a good agreement with the average residence time of the water molecules in the atmosphere.

Based on the validation with radiosonde observations, it can be concluded that the data processing facility is capable of providing tropospheric delay and PW estimates with sufficient accuracy to the EUMETNET E-GVAP project (Vedel 2006).

The investigations showed that the systematic bias of the PW estimations is mainly caused by the model used for the determination of the scale factor Q. Thus further refinement of the model is necessary to remove this systematic effect from the estimations. However it must also be noted that further independent observations should be used (such as microwave radiometers) in order to assess the performance of GNSS in the estimation of precipitable water vapour.

The results also showed the advantage of GNSS based PW estimations with respect to the radiosonde observations. GNSS is able to provide PW with a higher temporal and spatial resolution, which could lead to an improvement in predicting severe storms in the area of Hungary.

Acknowledgements The authors acknowledge the kindly support of the Hungarian Research Fund under the contract number K-83909. This study is linked with the "Development of quality-oriented and harmonized R + D + I strategy and functional model at BME" project. This project is supported by the New Hungary Development Plan (Project ID: TÁMOP-4.2.1/B-09/1/KMR-2010-0002). The authors would like to thank the comments of the three anonymous reviewers, their help to improve the quality of this paper is highly appreciated.

References

Aune B, Strabala KI, Lindstrom S, Huang A (2008) The direct broadcast version of the CIMSS regional assimilation system for global users. In: International EOS/NPP direct readout meeting 2008, Bangkok, 31 March–4 April 2008. http://dbmeeting.sci.gsfc.nasa.gov/files2008/DBCRAS_DB2008.ppt

Bevis M, Businger S, Herring TA, Rocken C, Anthes A, Ware R (1992) GPS meteorology: remote sensing of atmospheric water vapor using the global positioning system. J Geophys Res 97:15 787–15 801

Bosy J, Rohm W, Sierny J (2010) The concept of near real time atmosphere model based on the GNSS and meteorological data from the ASG-EUPOS reference stations. Acta Geodyn Geomater 7:253–263

Dach R, Hugentobler U, Fridez, P, Meindl M (2007) Bernese GPS software, version 5.0. Astronomical Institute, University of Bern

Emardson TR, Derks HJP (2000) On the relation between the wet delay and the integrated precipitable water vapour in the European atmosphere. Meteorol Appl 7:61–68

Essen L, Froome KD (1951) The refractive indices and dielectric constants of air and its principal constituents at 24 GHz. Proc Phys Soc (Lond) Sect B 64:862–875

Haase J, Maorong G, Vedel H, Calais E (2003) Accuracy and variability of GPS tropospheric delay measurements of water vapour in the western Mediterranean. J Appl Meteorol, Am Meteorol Soc 42:1547–1569

Igondova M, Cibulka D (2010) Precipitable water vapour and zenith total delay time series and models over Slovakia and vicinity. Contrib Geophys Geod 40:299–312

International Standard Organization (1975) Standard atmosphere. ISO 2533:1975

Karabatic A, Weber R, Haiden T (2011) Near real-time estimation of tropospheric water vapour content from ground based GNSS data and its potential contribution to weather now-casting in Austria. Adv Space Res 47:1691–1703

Kursinski ER, Hajj GA (2001) A comparison of water vapor derived from GPS occultations and global weather analyses. J Geophys Res 106:1113–1138

Nash J, Oakley T, Vömel H, Wei L (2011) WMO intercomparison of high quality radiosonde systems. WMO instruments and observing methods, report no. 107. p. 248

Pidwirny M (2006) The hydrologic cycle. In: Fundamentals of physical geography, 2nd edn (June 8, 2012). http://www.physicalgeography.net/fundamentals/8b.html

Rózsa S, Weidinger T, Gyöngyösi AZ, Kenyeres A (2012) The role of the GNSS infrastructure in the monitoring of atmospheric water vapor. Időjárás, Q J Hung Meteorol Serv 116(1):1–20

Saastamoinen J (1972) Contributions to the theory of atmospheric refraction. B Géodes 105(1):279–298

Saastamoinen J (1973) Contributions to the theory of atmospheric refraction. Part II. Refraction correction on satellite geodesy. B Géodes 107(1):13–34

Smith EK, Weintraub S (1953) The constants in the equation for atmospheric refractive index at radio frequencies. Proc IRE 41:1035–1037

Thayer GD (1974) An improved equation for the radio refractive index of air. Radio Sci 9:803–807

Vedel H (2006) E-GVAP meteorology and geodesy synergy. Presented at the EUREF symposium held in Vienna, 1–3 June 2005. http://egvap.dmi.dk/doc/presentations/egvap+euref.pdf

World Meteorological Organization (WMO) (2008) Guide to meteorological instrument and methods of observations. WMO-No. 8, p 681

Determining the 4D Dynamics of Wet Refractivity Using GPS Tomography in the Australian Region

Toby Manning, Witold Rohm, Kefei Zhang, Fabian Hurter, and Carl Wang

Abstract

The Earth's climate and weather is a highly dynamic and complex system. Monitoring and predicting meteorological conditions with a high accuracy and reliability is, therefore, a challenging task. Water vapour (WV) has a strong influence on the Earth's climate and weather due to the large energy transfers in the hydrological process. However, it remains poorly understood and inadequately measured both spatially and temporally, especially in Australia and the southern hemisphere. Four dimensional (4D) WV fields may be reconstructed using a tomographic inversion method that takes advantage of the high density of ground-based GPS Continue Operating Reference Station (CORS) networks. Recent development in GNSS tomography technique based on the dense Australian national positioning infrastructure has the potential to provide near real time 4D WV solutions at a high spatial and temporal resolution for numerical weather prediction, severe weather monitoring and precise positioning. This paper presents a preliminary study using the most advanced state CORS network—GPSnet as a test bed and introduces 4D GPS tomography in Australia and evaluates different parameters for voxel and height resolution and the influence of a priori data through simulations in a controlled field. Preliminary analyses of a real data campaign using a priori information are presented. These preliminary results conclude that the most optimal setup for GNSS tomography models in Victoria is: ~55 km horizontal resolution and 15 vertical layers with a smaller spacing in the lower troposphere and a larger spacing towards the tropopause. Further analysis will be undertaken to optimize the parameter settings for real data processing. The initial investigation into real data analysis has concluded an overall RMS error of 5.8 ppm with respect to the operational Australian Numerical Weather Prediction (NWP) model for 1 day.

Keywords

CORS • GPS • Meteorology • Tomography • Wet refractivity • WV

1 Introduction

GPS has been extensively used as a robust tool for measuring the integrated amount of WV in the atmosphere with high accuracy and under all weather conditions. It is currently regarded as one of the most important atmospheric remote sensing instruments for weather forecasting and climatology due to the rapidly increasing density of GPS CORS networks, the development of space-borne GPS technologies, and the

T. Manning (✉) • K. Zhang • C. Wang
Satellite Positioning for Atmosphere, Climate and Environment (SPACE) Research Centre, RMIT University, Melbourne, VIC 3083, Australia
e-mail: toby.manning@gmail.com

W. Rohm
Institute of Geodesy and Geoinformatics, WUELS, Wroclaw, Poland

F. Hurter
Geodesy and Geodynamics Laboratory, Institute of Geodesy and Photogrammetry, ETH Zurich, Zurich, Switzerland

C. Rizos and P. Willis (eds.), *Earth on the Edge: Science for a Sustainable Planet*, International Association of Geodesy Symposia 139, DOI 10.1007/978-3-642-37222-3_6,

continuous operability (Bevis et al. 1992; Rocken et al. 1995; Tregoning et al. 1998; Gradinarsky 2002; Bai 2005; Le Marshall et al. 2010). The capability of GPS tomography to reconstruct atmospheric wet refractivity fields has been proven in multiple studies using GNSS slant wet delays (SWDs) as the input observables (Flores et al. 2000; Nilsson 2005; Rohm and Bosy 2011; Van Baelen et al. 2011) and double difference (DD) SWDs (Nicholson et al. 2005; Troller et al. 2006; Lutz 2008; Perler et al. 2011). Current studies continue to assess the best methods to optimise the reconstruction process to ultimately attain robust algorithms with a high accuracy, reliability and near real time application.

Due to the sparse nature of ground-based atmospheric observation systems in the southern hemisphere the development of alternate methods for observing the spatial and temporal structure of the atmosphere is of high priority (Fu et al. 2009). Currently, the SPACE Research Centre at RMIT University and The Australian Bureau of Meteorology's longstanding joint collaboration has provided the research platform for the implementation of space-borne GPS meteorological information into the current NWP model (Le Marshall et al. 2010). This study aims to exploit the ground-based GPS infrastructure in Victoria and potentially other regions of Australia for the reconstruction of 4D WV distribution using GPS tomography. Detailed description of GPS signal refraction, GPS tomography principles and functional model of tomography is given in Sect. 2. The Victorian topography and atmosphere is a new area for tomographic analysis and thus a simulation study, shown in Sect. 3, is used as a first attempt to assess varying horizontal and vertical voxel resolutions and the influence of a priori data. Two synthetic horizontally homogeneous fields are used for the analysis (1) an exponentially decreasing wet refractivity field, and, (2) a spike wet refractivity field. The optimal parameters are then used for a preliminary analysis of real data, described in Sect. 4. This preliminary study is concluded in the Sect. 5, discussing implications of obtained results, presenting recommendations and showing further steps in the GPS tomography research. The outlook of this research will look at developing a robust tomographic platform providing high vertical and temporal wet refractivity data in near real time for numerical weather prediction models, severe weather prediction and precise positioning.

2 4D Modelling of Wet Refractivity with GPS Tomography

GPS satellite signals are delayed and bent due to the variations in refractive index as they propagate through different layers of the atmosphere to a ground receiver. A linear combination can effectively eliminate the ionospheric component leaving the dry and wet effects of the troposphere represented as refractivity (Rueger 2002).

$$N = 77.6890\frac{P_d}{T} + 71.295\frac{P_w}{T} + 375463\frac{P_w}{T^2} = N_{dry} + N_{wet}, \tag{1}$$

where N is the refractivity (ppm), P_d is the partial pressure of dry air (hPa), T is the atmospheric temperature (K) and P_w is the partial water vapour pressure (hPa). The first element of (1) is associated with dry refractivity N_{dry} whereas the last two with wet refractivity N_{wet}.

The GPS tomographic reconstruction process consists of retrieving the scalar field of wet refractivity values within a finite grid of volume pixels (voxels) from multiple integrated values passing through the media at different positions and orientations (Gradinarsky and Jarlemark 2004). The key aspect in GPS tomography is a linear relation between path delays which are an integrated measure of signal delay, and, refractivity N within the finite voxel model, the same relation holds. According to (1) for dry and wet refractivity, the integration of refractivity N along the propagation path delay Δ^{PD} between satellite x and receiver a can be expressed as (Troller et al. 2006):

$$\begin{aligned}\Delta^{PD}{}_a^x &= 10^{-6}\int_a^x N \cdot ds = 10^{-6}\int_a^x N_{dry} \cdot ds \\ &\quad + 10^{-6}\int_a^x N_{wet} \cdot ds = SHD + SWD,\end{aligned} \tag{2}$$

where ds is the line element along the ray path and SHD and SWD are slant dry and wet delays, respectively. Ray bending is neglected and a cut-off elevation angle of 5° is used (Bender et al. 2008).

The Bernese GPS processing software V5.0 is used to attain the Zenith Total Delays (ZTD) and the DD residuals $\Delta\Phi_{a,b}^{x,y}$ using a "shortest distance baseline" strategy and a double differencing approach (Dach et al. 2007). A DD path delay observation can be reconstructed between two satellites (x and y) and two receivers (a and b) using the ZTDs from the receivers which are mapped to the corresponding elevations of the satellites using the Niell mapping function (Niell 1996) $m\left(el_{rec}^{sat}\right)$ with the addition of DD residuals. In this study the wet refractivity is of interests, therefore the dry component is eliminated with high accuracy using additional ground meteorological observations at the GPS station using the dry Saastamoinen model (Saastamoinen 1972). The final DD SWD equation (Troller et al. 2006) reads as follows:

$$\Delta^{2,\,SWD}{}_{a,b}^{x,y} = \overline{\Delta^{2,SWD}{}_{a,b}^{x,y}} + \Delta\Phi_{a,b}^{x,y}, \tag{3}$$

where,

$$\overline{\Delta^{2,SWD^{x,y}}_{a,b}} = \left(\overline{\Delta_b^{ZWD}} \cdot m\left(el_b^x\right) - \overline{\Delta_a^{ZWD}} \cdot m\left(el_a^x\right)\right) - \left(\overline{\Delta_b^{ZWD}} \cdot m\left(el_b^y\right) - \overline{\Delta_a^{ZWD}} \cdot m\left(el_a^y\right)\right). \quad (4)$$

DD SWDs are constructed and used as the input views through the finite voxel model due to the advantage of automatically eliminating the satellite and receiver clock biases (Ware et al. 1997).

For this study, the 4D WV tomography is processed using the Atmospheric Water Vapour Tomography Software 2 (AWATOS 2) which uses a Kalman filter for the forward processing, pseudo-inverse and inter-voxel constraints (Perler 2011). Using a triliniear parameterized field the algorithm of AWATOS 2 expresses the DD SWD observations as a weighted sum of the grid nodes (Perler et al. 2011).

$$\Delta^{SWD} = 10^{-6} \sum\nolimits_i \int_{s_i}^{s_{i+1}} N_{wet,i}\, \Delta s_i \quad (5)$$

The tomography system of Eq. (5) is solved for wet refractivity using additional constraints in the form of pseudo observations, and optional a priori observations $N_{apriori}$ such as radiosonde or ground-based meteorological sensors, GPS radio occultation and radiometers. In the matrix form Eq. (5) with additional information as stated above, reads as follows (Lutz 2008):

$$\begin{pmatrix} \Delta^{2,SWD^{x,y}}_{a,b} \\ ZWD_a \\ N_{apriori,i} \\ 0_i \end{pmatrix} = H \cdot \begin{pmatrix} N_{wet\ 1} \\ N_{wet\ 2} \\ N_{wet\ 3} \\ N_{wet\ 4} \\ N_{wet\ 5} \\ N_{wet\ 6} \\ \cdots \end{pmatrix}. \quad (6)$$

Where H is the design matrix. The Kalman filter is a powerful processing procedure and is highly advantageous for estimating the evolution of dynamically changing parameters. Previous studies have also incorporated a Kalman filtering technique to efficiently utilize the slant delay observations to attain tomographic solutions (Gradinarsky and Jarlemark 2004; Nilsson 2005; Troller et al. 2006; Perler et al. 2011). Without loss of generality Kalman filter equations in epoch k, adapted to comply with notation presented before read as follows (Grewal and Weill 2002):

Predicted state vector:

$$\hat{N}_{wet\ k}\,(-) = \mathbf{F}_k \hat{N}_{wet\ k-1}(+) \quad (7)$$

Prediction covariance matrix:

$$\mathbf{P}_k\,(-) = \mathbf{F}_k \mathbf{P}_{k-1}(+)\mathbf{F}_{k-1}^T + \mathbf{Q}_{k-1} \quad (8)$$

Updated state estimate:

$$\hat{N}_{wet\ k}\,(+) = \hat{N}_{wet\ k}\,(-) + \overline{\mathbf{K}}_k \left(z_k - \mathbf{H}_k \hat{N}_{wet\ k}\,(-)\right) \quad (9)$$

Update covariance matrix:

$$\mathbf{P}_k\,(+) = \mathbf{P}_k\,(-) - \overline{\mathbf{K}}_k \mathbf{H}_k \mathbf{P}_k\,(-) \quad (10)$$

With the Kalman gain:

$$\overline{\mathbf{K}}_k = \mathbf{P}_k\,(-)\,\mathbf{H}_k^T \left(\mathbf{H}_k \mathbf{P}_k\,(-)\,\mathbf{H}_k^T + \mathbf{R}_k\right)^{-1} \quad (11)$$

Where, Q_k reflects the dynamic disturbance noise, z_k is a matrix containing all types of observations as stated in (6), P_k is the covariance matrix, F_k is the transition matrix, R_k is a measurement noise, and $\hat{N}_{\text{wet k}}\,(-/+)$ is the predicted and updated state, respectively.

Following Perler et al. (2011) the transition matrix F_k in AWATOS 2 is implemented as the identity matrix. The initial state provided from the background model is predicted with (7) and updated with (9) based on the Kalman gain matrix $\overline{\mathbf{K}}_k$ (11) in every estimation step. The procedure also applies to prediction (8) and update (10) of the covariance matrix. The initialization of the Kalman filter follows parameters set in AWATOS 2 from Perler (2011).

3 GPS Tomography Simulations

The feasibility and capability of reconstructing the physical dynamics of wet refractivity using a 4D tomographic technique above the topography of Victoria, Australia is initially tested using simulations of a synthetic tropospheric state. The simulations are then used as a preliminary evaluation for the horizontal and vertical voxel resolution, and, to assess the influence of a priori data on the solution convergence rate and solution accuracy. Future studies will focus on developing a scientific platform for near real time tomographic data in Australia. The Victorian GPS CORS network comprises approximately 105 dual-frequency geodetic grade GPS receivers in continuous operation from which 76 are used for this research. Mean inter-station distance is approximately ~55 km with a reasonably homogeneous distribution. The network is highly dense for Australian standards and has the potential to be a major resource for meteorological data especially in the absence of sufficient meteorological observation systems. The initial voxel construction was set to a standard 1° (110 km) horizontal voxel resolution. A mean GPS inter-station distance of 55 km for GPSnet was adopted as the horizontal resolution following conclusions of

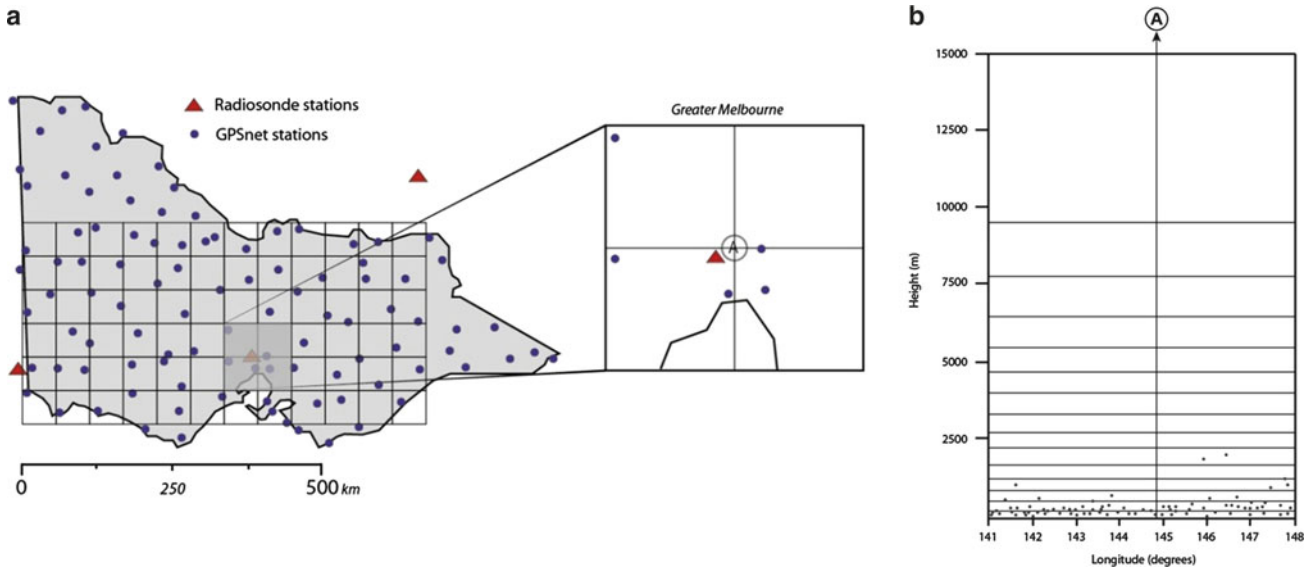

Fig. 1 3D view of the tomographic voxel model showing the first six layers (**a**). And, plan view of the GPSnet network and voxel model (**b**). Voxel corner point (A) is used for profile analysis

preconditions for GPS tomography from Bender and Raabe (2007). A final configuration of 27.5 km resolution was also tested to identify the limitations of a higher horizontal resolution, useful for analysis of severe multi cells storms, super cell storms and tropical cyclones (Ahrens and Samson 2010). Figure 1 shows the current Victorian GPSnet infrastructure and locations of sites under experiment and the base 6×12 voxel model (55 km resolution). In this analysis the voxel corner point A is used for validation purposes of the reconstructed refractivity field (Fig. 1).

3.1 Experiment Setup

Each simulation campaign is processed using real ground GPS station and satellite coordinates. Two synthetic horizontally homogeneous fields are used for the analysis (1) an exponentially decreasing wet refractivity field averaged from a radiosonde profile from 1st December 2010, and (2) a spike wet refractivity field (Perler 2011).

There is no variation in the horizontal as the main limitation in GPS tomography is the vertical resolvability (Perler 2011; Rohm and Bosy 2011). For simulations based on a synthetic exponentially decreasing wet refractivity field the following expression is used (Perler 2011):

$$N_{wet}(h) = N_{wet\,0} \exp\left(-\frac{h}{h_s}\right), \tag{12}$$

Where, $N_{wet\,0}$ is the surface wet refractivity and h_s is the scale height. To assess the impact of the vertical layer spacing on the tomographic solution two different segmentation techniques were used, namely constant and exponentially decreasing resolutions. Figure 3 presents the height distribution of GPSnet stations with respect to both layer spacing techniques.

A flat distribution of GPSnet stations is evident with only 8 stations above 500 m altitude and a maximum station height of ∼1,900 m. Large variations in receiver heights are essential for resolving the vertical structure using tomography (Bender and Raabe 2007). With the absence of optimal receiver geometry, inter-voxel constraints and additional information on the vertical profile of refractivity become increasingly more important (Gradinarsky and Jarlemark 2004). Current experiments adopt two different vertical spacing techniques—constant (Rohm and Bosy 2011) and exponential (Champollion et al. 2005; Lutz 2008; Perler 2011). This preliminary study aims to compare both methods using the same number of layers which corresponds to the same number of unknowns in (6). The exponential spacing technique distributes the stations over 7 lower layers creating a height differential which in theory will enhance the vertical resolvability compared to the constant technique which hold nearly all stations in the bottom layer.

Next step was to assess the influence of additional point observations $N_{apriori}$ on the tomographic solution. Two methods are tested (1) the $N_{apriori}$ represents simulated data for a network of synoptic weather stations, and, (2) the $N_{apriori}$ represents a simulated profile located in the centre of the model. Both methods derive observations from simulated wet refractivity field (12) and are input into the observation matrix equation set (6) as a known value with a variance of 1 ppm^2 at point $(p_{\phi,\lambda,h})$.

The evolution of the simulated tomographic reconstruction process uses a forward and backward modelling strategy. Firstly, an initial synthetic refractivity field (original field) is defined. In the forward model process, ray tracing

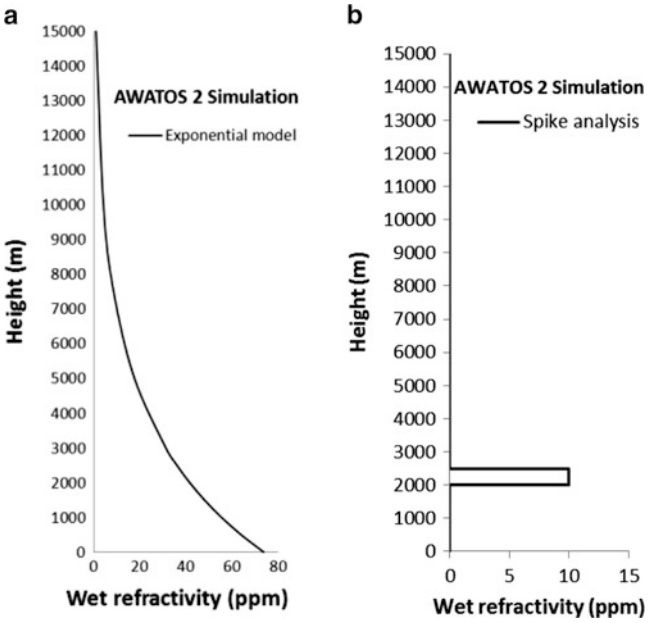

Fig. 2 Exponentially decreasing refractivity field (**a**), spike refractivity field (**b**)

Table 1 Table presenting the optimal configuration and the experiment variations

Voxel resolution	Base configuration	Experiment variations
Horizontal	6 latitude × 12 longitude	3 × 6, 6 × 12, 12 × 24
Vertical	15 levels	15
Vertical layer spacing	Exponential function	Constant, exponential function

Table 2 Observation model parameters

Observation model parameters	Value
GPS observations	Double difference slant wet delays
Number of GPS stations	74 (∼105 *in GPSnet*)
Inter-station distance (km)	∼55
GPS sampling interval size (s)	30
Tomography step size (s)	30
Additional observations	None
Observation covariance matrix	Full covariance model

implemented in the AWATOS2 software (Perler et al. 2011) is used to simulate integral *SWD* (2) and point observations through the synthetic atmosphere (12), as shown in Fig. 2. At this stage measurement noise is added to the simulation process using a Gaussian distribution error of 5 mm in the zenith direction. This accuracy measurement is extracted from final results of a validation study comparing ZPD estimates of three GPSnet receivers to three Victorian radiosonde sites over a 2 month period (December 2010–January 2011) and complies with the value used in (Perler 2011). Afterward, observations including satellite and receiver coordinates are used to reconstruct DD SWD observations table 2. The simulated observation data is then used to reconstruct the refractivity field using the Kalman filter (7–11)—this is the backward model process. Finally, the estimated field $\hat{N}_{wet}$ is compared to the simulated atmosphere N_{wet}. The step size of the backward model (9) and observation sampling size are both set to 30 s. The data evaluation process uses a profile comparison at voxel corners (A), since our focus lies on resolving the vertical structure. The root mean square (RMS) error of the difference between simulated N_{wet} profile at (A) and estimated wet refractivity profile at (A) is used to assess the accuracy of the profile solution. Additionally, the solution convergence rate and processing time are also taken into account.

3.2 Results and Discussion

Horizontal Resolution

The high horizontal voxel resolution is an imperative parameter for optimizing the depiction of highly dynamic hydrological hazards (Lutz 2008). The horizontal distribution of wet refractivity is highly variable in space and time especially during the life cycle of severe weather. The development of an optimal configuration for detecting the dynamic changes in wet refractivity in Australia is a goal for future research with potential applications in nowcasting, severe weather and precise positioning. This preliminary study compares the tomographic solution accuracy of three horizontal voxel resolutions (Table 1) using the exponentially decreasing wet refractivity state 2(a). The objective is to identify which horizontal voxel spacing is optimal for reconstructing the 4D structure of wet refractivity based on solution convergence rate, RMS error analysis and total processing time. A 3×6 configuration (110 km resolution) was used in an initial tomographic simulation. The second simulation followed Bender and Raabe (2007) where the mean GPS inter-station distance of ∼55 km was adopted (6×12). The final 27.5 km resolution was constructed as double the second resolution (12×24) to assess a higher resolution, advantageous for severe weather monitoring (Ahrens and Samson 2010). For all three horizontal resolutions vertical layer spacing is kept fixed to the exponential model (Fig. 3a). Figure 4 presents the RMS error for each configuration over the first hour. The 55 km solution converges below 1 ppm within 13 min and has a final RMS error of 0.49 ppm after 24 h. The 110 and 27.5 km solutions take 45 and 40 min respectively to converge below an RMS error of 1 ppm and conclude a final RMS error of 0.20 and 0.78 ppm respectively. The total processing time for this 24 h campaign using 27.5, 55 and 110 km, solutions were 10 h, 24 h and 5 weeks respectively.

Based on these initial results the 55 km horizontal resolution was concluded to be optimal as the convergence rate was faster than the 27.5 and 110 km solutions by more than

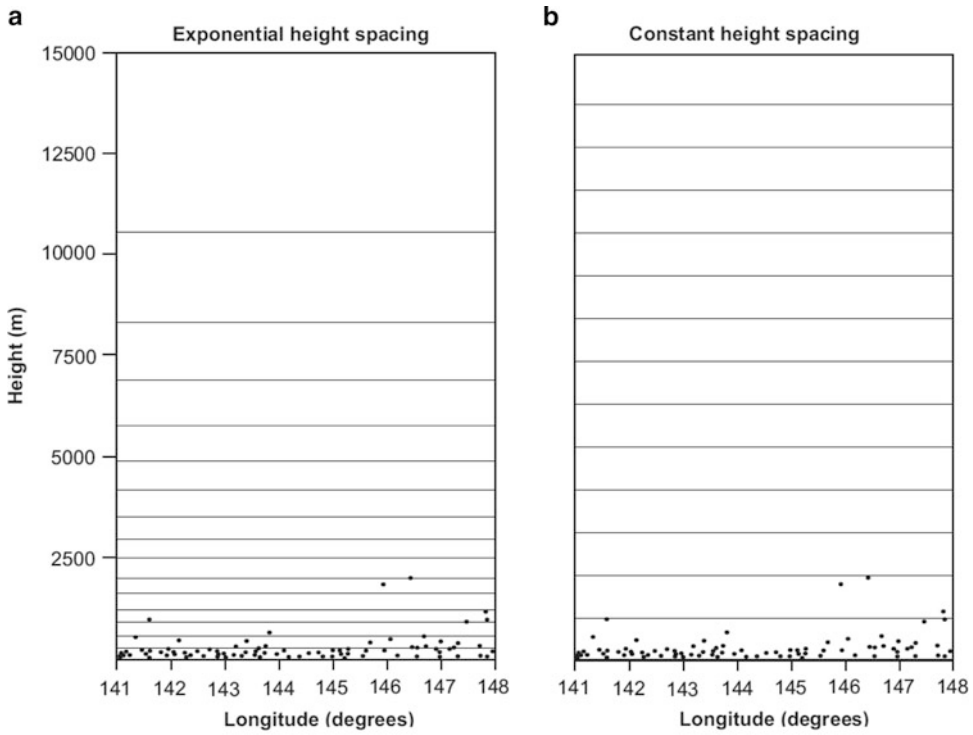

Fig. 3 Height distribution of GPSnet stations represented in of (**a**) exponential height spacing function, and of (**b**) constant height spacing

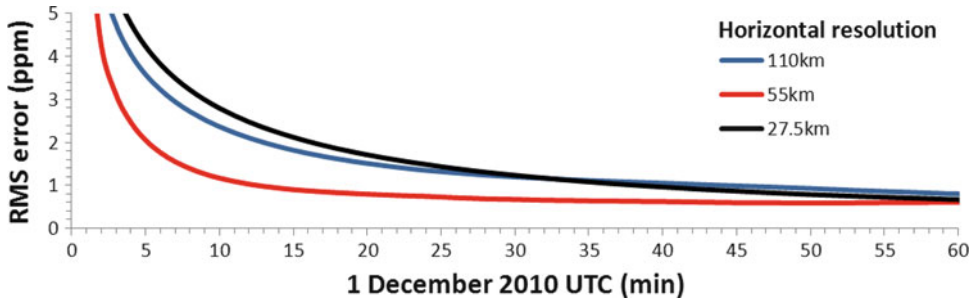

Fig. 4 Comparison of the RMS error of tomography solutions for 27.5, 55 and 110 km horizontal resolutions presenting the first 60 min of processing

a factor of 3. The processing time of the 55 and 110 km solutions were both equal to, or, less than the total campaign time which is sufficient for the scope of near real time solutions. The 27.5 km resolution was disregarded due to the processing time taking 35 times longer than the 55 km solution and the slow convergence as seen in Fig. 4.

Vertical Resolution

Up to 50 % of water vapour is located in the boundary layer. It is therefore, imperative to model the dynamic and vertical structure of water vapour below ∼2 km with high resolution. This paper presents results from a simulation study on the vertical resolution, testing the feasibility of reconstructing a sharp vertical wet refractivity spike within a defined vertical layer (Perler 2011; Rohm and Bosy 2011). This analysis uses a constant wet refractivity field of 0 ppm and implements a wet refractivity spike layer of 10 ppm from 2,000 to 2,500 m altitude situated ∼100 m beyond the altitude of the highest ground station. It compares two layer spacing techniques: constant and exponential spacing (Fig. 3). A total of 15 layers are used for each voxel spacing technique providing 1 km vertical grid spacing with the constant method and high to low vertical resolution with increasing altitude for the exponential method. DD SWD observations are simulated through the spike refractivity field (Fig. 2b).

Figure 5a presents the profile comparison between constant and exponential spacing after 20 min of processing. Both configurations produce a similar RMS of 2 ppm after 20 min, however it can clearly be seen that the exponential method has a much higher vertical resolution in the lower troposphere (< 5 km altitude) in contrast to the constant method and much less in the upper troposphere (up to 15 km). In this respect the exponential technique is advantageous as it provides high resolution at low altitudes where the density of water vapour is high and lower resolution in the upper layers where there is exponentially less. This conclusion is consistent with Lutz (2008) and Perler (2011). Figure 5b presents the convergence of the solution over time with the

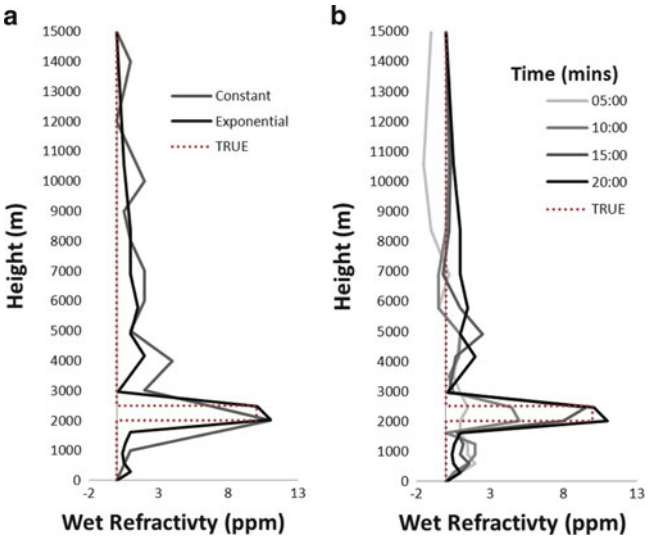

Fig. 5 Spike layer profile comparison between constant and exponential vertical spacing configurations (**a**), and time evolution of spike layer analysis using exponential vertical spacing configuration (**b**)

spike being accurately resolved after 20 min of processing using a time step and data interval size of 30 s. The optimum number of layers are yet to be determined, currently 15 layers in exponential scheme is set to comply with 1 km vertical resolution from constant method.

Additional Point Observations

Using evidence presented in this section the 55 km grid model and exponential layer function are used as the optimal grid structure. Two types of additional data are processed and compared using identical forward and backward simulation processing parameters. The first simulates the use of synoptic weather station networks within Victoria. The second simulates the inclusion of profile observations such as radiosonde and GPS radio occultation (Hajj et al. 2002). For both methods point meteorological data ($N_{apriori}$) are simulated for each station or profile point ($p_{\phi,\lambda,h}$) using (12) with a variance of 1 ppm^2 and included into the observation matrix in (6). The objective of this simulation is to identify the magnitude of influence additional data has on the solution with respect to convergence time and final RMS error accuracy. The data sampling rate for the synoptic and profile data was set to 15 min and 12 h respectively, to simulate Australian standards.

The synoptic solution converged to an accuracy of less than 1 ppm within 4 min with a final RMS error of 0.22 ppm, whereas, the profile solution converged to an accuracy of less than 1 ppm within 3 min with a final RMS error of 0.1 ppm. Compared to the solution without additional data the convergence rate for the synoptic and profile solution are faster by a factor of 3 and 4 respectively.

In addition, further developments are proposed to include both synoptic and profile data from instruments such as radiosonde and GPS radio occultation for real data campaigns. These will have significant influence on the vertical resolvability and the tomographic solution's ability to track sharp temporal changes in highly dynamic wet refractivity fields especially during the lifecycle of severe weather.

4 Preliminary Real Data Experiment

This preliminary real data experiment is conducted for 24 h on the 1st December 2010 under unstable conditions of severe weather. Hail, heavy rain and thunderstorms were all reported throughout Victoria during the 24 h campaign. GPS data from the Victorian GPS network (Fig. 2) was processed using the Bernese GPS processing software V5.0 (Dach et al. 2007) using a shortest distance baseline strategy and a double difference approach. The estimated hourly Zenith Path Delay (ZPD), the DD residuals, interpolated meteorological data from Numerical Weather Prediction model ACCESS-R (Le Marshall et al. 2010) and satellite and receiver coordinates are used to reconstruct the DD SWD (3) observations which are the primary input for the tomography inversion during each update step (7–11). Furthermore, an exponentially decreasing wet refractivity field (12) is used as the initial state. A 55 km voxel model is used with a 15 increasingly larger height layers. This preliminary study restricts the experiment to 1 day with update solutions every 5 min.

Each 6 hourly NWP analysis profile is compared to the tomographic solution with a final RMS error of 5.8 ppm. Figure 6 shows the evolution of the tomographic profile (A) up to 7,500 m throughout the 24 h with the indication of sharp temporal changes detected. The profile on the right (Fig. 6) presents the average profile for the 24 h and the standard deviation of wet refractivity at different heights. It can be seen that the largest amount of variation occurs below 3,000 m which provides the emphasis for higher resolution in lower layers. Continuing research will focus on the accurate implementation of additional a priori information from modern atmospheric sounding technologies such as GPS RO and radio sounding.

5 Conclusion and Outlook

The results presented in this paper show a new study into methods of discretizing the atmosphere in the Victorian region using a 4D GPS tomography solution processed with the AWATOS2 software package (Perler et al. 2011). The SPACE Research Centre in collaboration with the BoM are currently involved in researching sophisticated methods of

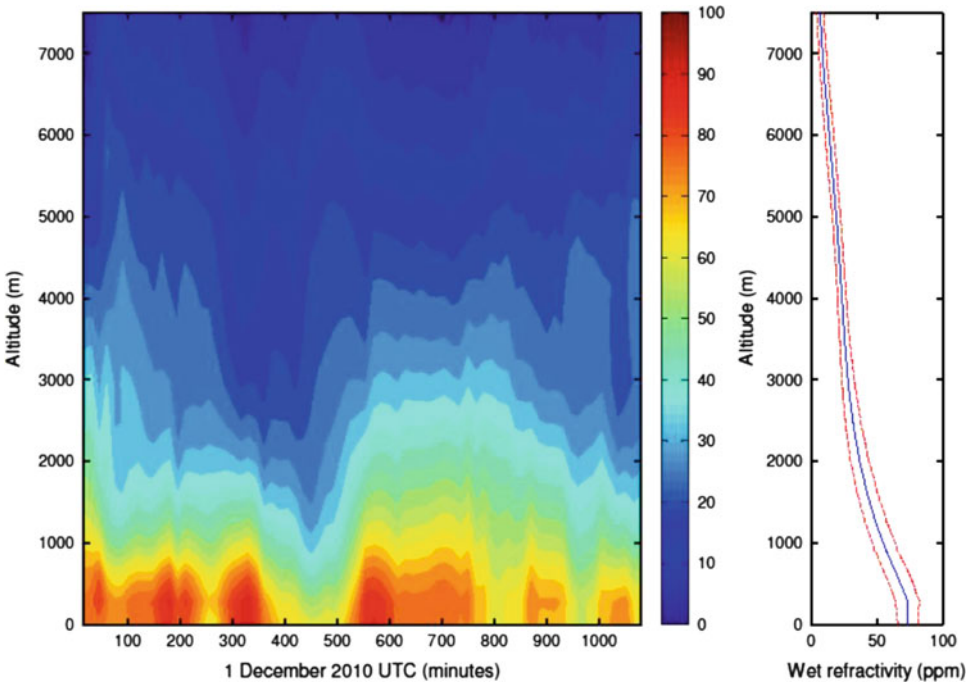

Fig. 6 Wet refractivity profile for 24 h (1st December 2010). The figure shows the temporal change of a wet refractivity profile (A) every 5 min with the profile on the right presenting the average profile and standard deviation of the daily wet refractivity at different heights

implementing space-borne GPS meteorological information into the BoM NWP model (Le Marshall et al. 2010). Ground-based GPS observations as critical Australian National Positioning Infrastructure have not yet been incorporated into the operational NWP ACCESS-R model. This preliminary study provides the platform for continuing developments in 4D GPS tomography and ultimately aims at deriving an optimized algorithm of tomography within Australia to increase the capability of NWP model forecasts, nowcasting and especially in the early detection of severe weather events. A simulation study is used to compare solution accuracies of varying horizontal and vertical voxel resolutions and the influence of a priori data. This preliminary investigation revealed an optimal voxel construction of 55 km horizontal resolution with 15 increasing height layers based on convergence rate, final RMS error and data processing time. Further simulations showed the addition of a priori information has a large influence on the vertical resolvability and convergence rate of tomographic solutions. Future simulation research will be focused on conclusive parameter optimization for the Australian region. Preliminary real data analysis assessed the time evolution of tomography solutions over 24 h with an overall RMS error of 5.8 ppm compared with Australian NWP analysis. Further real data research will aim at incorporating sophisticated a priori observation methods such as GPS RO and radiosonde into the tomography to assess the improvements in the resulting refractivity fields and the potential future capability of assimilating solutions into the Australian NWP model to analyze forecast improvements.

Acknowledgements This project is supported by the Australian Space Research Project (ASRP) and the Australian Research Council (ARC) Linkage (LP0883288) project both funded by the Australian Federal Government. We also thank the Geodesy and Geodynamics Lab, ETH Zurich, Switzerland for providing the AWATOS 2 software package, the Australian Bureau of Meteorology for providing the synoptic weather station and radiosonde data, and, the Department of Sustainability and Environment for providing the GPSnet data.

References

Ahrens D, Samson P (2010) Extreme weather and climate. Brooks/Cole Pub Co/Cengage Learning, Belmont

Bai Z (2005) Near-real-time GPS sensing of atmospheric water vapour. PhD Thesis, Queensland University of Technology

Bender M, Raabe A (2007) Preconditions to ground-based GPS water vapour tomography. Ann Geophys 25(8):1727–1734

Bender M, Dick G, Wickert J, Schmidt T, Song S, Gendt G, Ge M, Rothacher M (2008) Validation of GPS slant delays using water vapour radiometers and weather models. Meteorol Z 17(6):807–812

Bevis M, Businger S, Herring T, Rocken C, Anthes R, Ware R (1992) GPS meteorology: remote sensing of atmospheric water vapor using the global positioning system. J Geophys Res 97:15787–15801

Champollion C, Mason F, Bouin M, Walpersdorf A, Doerflinger E, Bock O, van Baelen J (2005) GPS water vapour tomography: preliminary results from the ESCOMPTE field experiment. Atmos Res 74:253–274

Dach R, Hugentobler U, Fridez P (2007) Bernese GPS software version 5.0. Astronomical Institute, University of Bern, Bern

Flores A, Ruffini G, Rius G (2000) 4-D tropospheric tomography using GPS slant wet delays. Ann Geophys 18:223–234

Fu E, Zhang K, Marion K, Xu X, Marshall J, Rea A, Weymouth G, Kuleshov Y (2009) Assessing COSMIC GPS radio occultation derived atmospheric parameters using Australian radiosonde